J. Fluid Mech. (1972), *vol.* 53, *part* 2, *pp.* 351–383
Printed in Great Britain

Microscale pressure fluctuations measured within the lower atmospheric boundary layer

By J. A. ELLIOTT

Institute of Oceanography, University of British Columbia†

(Received 18 June 1971 and in revised form 20 November 1971)

Eulerian measurements of microscale fluctuations in static pressure are used, in conjunction with measurements of air velocity, to describe some of the properties of the static pressure fluctuations that occur within the turbulent flow of the lower atmospheric boundary layer. Using an instrument developed to measure the static pressure at a point within the boundary layer, data were collected at heights ranging from the surface up to about 6 m. The results are presented as power spectra, cross-spectra, coherence and phase. For all observations over a flat boundary the root-mean-square pressure produced by the boundary-layer turbulence is about 2·6 times the mean stress. The pressure spectra are found to have a well-defined shape which does not change with height above the surface; at the higher frequencies the spectra show a power-law behaviour with a mean slope of $-1{\cdot}7$. A number of observations with two pressure sensors are used to describe the structure and propagation velocity of individual pressure pulses.

A dominant feature of the pressure–velocity relationship is that the large-scale pressure fluctuations are approximately in phase with the downstream velocity fluctuations; at small scales there is a large phase difference ($\simeq 135°$). These phase differences are interpreted to be the result of interaction of the large pressure-producing scales with the earth's surface, the small scales being 'free' of the surface. From the simultaneous measurements of pressure and downstream velocity the effect of pressure forces on the energy flux out of the downstream velocity fluctuations was evaluated. Typical values are about 0·45 of the net energy source to the downstream component. By means of pressure and vertical velocity measurements an estimate of the pressure divergence term in the net energy budget of a boundary layer is made. It was found to be about $\frac{1}{10}$ of the energy feeding term.

1. Introduction

Experimental observations of fluctuations in the static pressure that occur in a turbulent boundary layer have, except for one example (Gossard 1960), been confined to the measurement of these fluctuations at the surface, either of the earth or of a wind tunnel. Recently, at the Institute of Oceanography, University of British Columbia, an instrument that provides a reliable Eulerian measurement of static pressure at a point within the atmospheric boundary

† Present address: Bedford Institute, Dartmouth, Canada.

layer was developed. The instrument was used in this study to examine some of the kinetics and kinematics of turbulent boundary-layer pressure fluctuations from measurements at various heights above the boundary.

As shown by previous work (e.g. Gossard 1960; Herron, Tolstoy & Kraft 1969) the spectra of atmospheric pressure fluctuations measured near the surface do not exhibit the 'mid-frequency' minimum commonly found in velocity spectra (see Fiedler & Panofsky 1970) but generally decrease continually in intensity from the low frequency synoptic pressure fluctuations to the higher frequency pressure fluctuations associated with the boundary-layer turbulence. One of the possible sources of these 'mid-frequency' fluctuations is internal gravity waves at higher elevations (Herron *et al.* 1969). Since the spectra of atmospheric pressure fluctuations cannot easily be separated into a microscale and mesoscale range, the microscale range in this study is defined from the velocity spectra and is taken to be the same range of scales as is found in the turbulent velocities in the lower few metres of the atmosphere.

Some aspects of this microscale range have been examined in detail by Priestley (1965), Golitsyn (1964) and Gorshkov (1967, 1968) using surface observations. Priestley employed an array of surface sensors to evaluate the longitudinal and lateral correlation coefficients. The work by the two Russian authors is mainly on spectra and some pressure velocity cross-spectra.

Starting with the work of Willmarth (1958) there have been several wind tunnel experiments involving surface pressure measurements; recent examples are Bull (1967) and Blake (1970). Some of the conclusions from these studies are: (i) that the measured r.m.s. wall pressure is fairly well established at about 3 times the wall shear stress, (ii) that the advection speed of the pressure fluctuations is about 0·6 to 0·85 times the stream speed, (iii) that the pressure-producing eddies of wavelength λ decay after travelling a distance of a few λ and (iv) that the transverse scales and longitudinal scales of pressure fluctuations measured at the wall are approximately the same size.

Though the atmospheric boundary layer does not have a completely uniform surface nor a steady mean flow, sites and winds were chosen to keep inhomogeneities at a minimum so that the data obtained would represent as closely as possible a fully developed homogeneous turbulent boundary layer.

2. Experimental and analytic techniques

2.1. *Sites*

The observations were taken at two sites: Spanish Banks and Ladner; both are located in the vicinity of Vancouver, British Columbia. The Spanish Banks site, described previously by Pond *et al.* (1966), is on a tidal flat on the south side of English Bay. Most observations were taken when the water was either absent or very shallow, leaving a surface of sand or water with small waves of wavelength less than half a metre. The area beyond the 0·5 km wide tidal flat is water, with fetches of 7–50 km. On four occasions measurements were taken when the water was relatively deep and larger waves were present. For these four 'runs', the observations were taken sufficiently high above the waves for the

spectra not to show any influence from the waves (as found in observations taken closer to the waves) and they agree with the results obtained when no waves were present. The Ladner site is on a 40 metre wide taxiway near the centre of an abandoned airport located on the Fraser River Delta south of Vancouver. The terrain between the asphalt runways and taxiway and for about 1 km immediately surrounding the airport was mainly thick grass 10–30 cm high. The area adjacent to the airport consists largely of flat cultivated farm land. For the observations obtained at this site the wind blew from the west, perpendicular to the taxiway; measurements were taken about 30 m from the leading (windward) edge. At both sites typical wind speeds were between 5 and 10 m s^{-1}.

2.2. *Instrumentation*

The static pressure fluctuations were measured using the University of British Columbia system, described in detail by Elliott (1970). The critical part of the design of the instrument is the shaping of a probe. The probe, consisting of a thin streamlined circular disk at the end of a long stem, was developed empirically from wind tunnel studies. It is shaped such that when it is held fixed within the turbulent flow of the atmospheric boundary layer the fluctuations in dynamic pressure that arise from the air being deflected around the probe are small when compared with the fluctuations in the static pressure of the undisturbed turbulent flow. The pressure is sampled at ports located at the centre of the disk which are connected directly via the stem to a commercial differential pressure transducer. The reference for the transducer is a vacuum flask. Figure 1 (plate 1) is a view of the instrument from above. During normal operation, the stem is aligned with the mean wind. The length of the stem is such that it places the disk beyond significant interference from the transducer container or the brackets used to hold the instrument.

Two methods were used to test the ability of the probe to operate in a fluctuating flow. In the first, a wind tunnel test, the expected wind fluctuations were simulated by either holding the probe at different fixed alignments with respect to the mean flow or by changing the speed of the flow while the probe was aligned with the flow. Any mean change in the pressure observed by the probe relative to the static reference of the tunnel was taken to be the unwanted dynamic pressure. This test showed that, for the range of angles and downstream wind fluctuations expected within the atmospheric boundary layer under conditions of neutral stability, the dynamic pressure sensed by the probe changed by values between 0·001 and 0·002 of the mean stagnation pressure. When compared with an expected magnitude for fluctuations in static pressure of about 0·01 of the stagnation pressure, the probe would have had a signal-to-noise ratio of about 5:1. The other method used as a test was to compare the signal obtained from the new instrument with that obtained simultaneously from the more reliable surface-port method. The arrangement used is illustrated in figure 2. The signals from the two sensors were then compared for similitude at scales large compared with the separation. The range of angles between the direction of the mean and fluctuating flow at a height of 30 to 40 cm will be similar to those at any height within the constant stress layer provided that the flow is neutrally

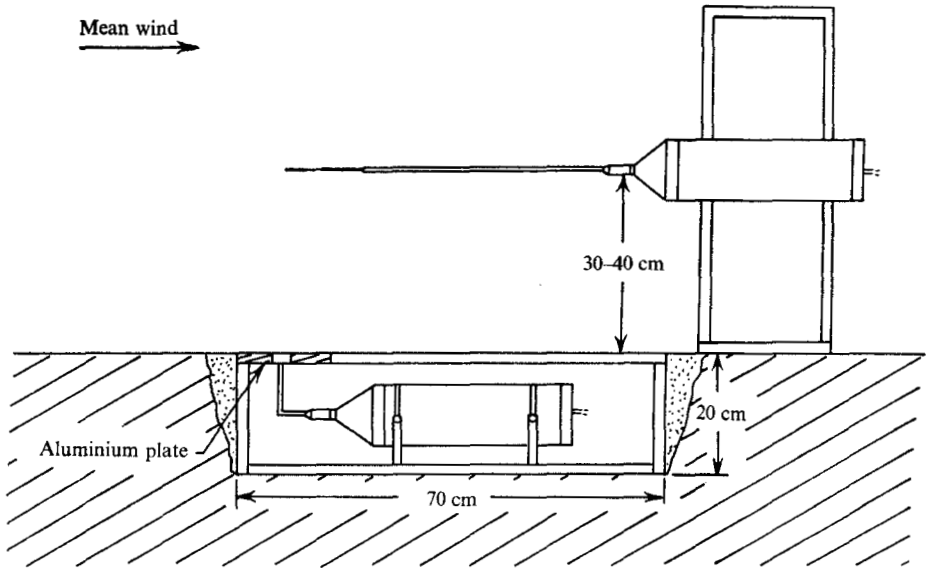

FIGURE 2. Arrangement used for comparing the pressure fluctuations sampled by the probe with those sampled by a surface port.

stable. Numerous tests were conducted using this arrangement and encompassing a variety of surface conditions and wind speeds, each test lasting about half an hour. An example of the spectra and of the coherence and phase between the two signals is shown in figure 3 (analysis discussed below). The power spectra agree to within about $\pm 20\%$ ($\pm 10\%$ in amplitude) over the high coherent range, with phases the same to within $\pm 5°$. The sites and atmospheric conditions for this latter test were similar to those encountered during all other data collection.

The instruments were designed to respond to a frequency range of 0·003–20 Hz. The high frequency end was limited by the small passages of the probe; the low frequency end was adjusted by a small slow leak between the two sides of the differential pressure transducer. The frequency response was measured by using an oscillating pressure source at the input of the probe and comparing the signal measured by the instrument with that from the source. The accuracy of this calibration is about $\pm 2\%$ in amplitude and $\pm 3°$ in phase. All data presented below were corrected for instrument response.

Turbulent velocity measurements were taken in conjunction with the pressure measurements. Two different instruments were used for this purpose: the Kaijo Denki three-dimensional acoustic anemometer (sonic) with a 20 cm probe path length, and the Disa constant-temperature anemometer (U-wire). The turbulence sensors were mounted on vertical masts at various heights, all below 6 m. Analog signals from the instruments were transmitted by cable to a central location where they were recorded in FM analog form on magnetic tape using an AMPEX FR-1300 tape recorder.

A mean wind speed profile was measured with cup anemometers, normally positioned with a logarithmic spacing at levels between 0·5 and 5 m. The cup

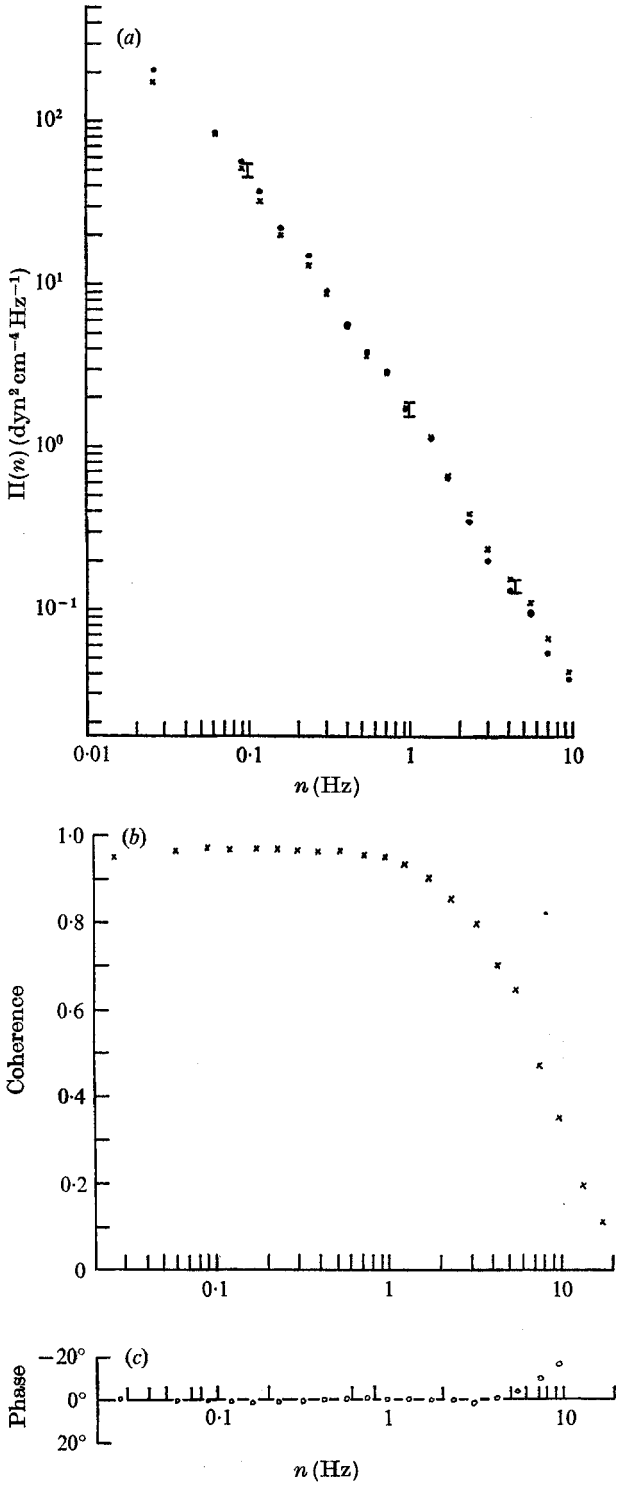

FIGURE 3. Static pressures measured in the air and at the surface; the separation was 32 cm vertically. This measurement was taken at the Ladner site. (*a*) Spectral comparison: ×, sensor in the air; ●, sensor at the surface; I, 95 % confidence limits. (*b*) Coherence. (*c*) Phase.

system is of the counter type and was read at timed intervals. The mean wind at any level was obtained graphically using a best-line fit to the cup readings plotted on a log–linear plot. For observations over water, the winds have been referred to a co-ordinate system moving with the mean current. Results are accurate to within $0{\cdot}1\,\mathrm{m\,s^{-1}}$.

In addition to the cup anemometer data, other information logged manually included wind direction, wet and dry bulb temperatures, water temperatures, currents and mean water level, where applicable.

2.3. *Analysis*

An attempt was made to take observations only for a steady mean wind and direction, for neutral stability and over a homogeneous flat terrain, since these were the assumptions used in analysing the data. In practice, observations were analysed only when the mean wind speed and direction were later found to be reasonably steady over a period of approximately 30 min; if a 5 min average wind speed changed by more than 20–30 % from the previous 5 min average, conditions were considered to be non-stationary and the data were not used. In the usual manner the 'frozen field' (Taylor's) hypothesis is assumed. This gives the relationship between frequency n and wavenumber k as $k = 2\pi n/U = \omega/U$, where U is the mean advection wind (in the case of pressure fluctuations it is the propagation rate of the pressure fluctuations U_p). The same assumption allows phase shift corrections to be made and horizontal gradients to be calculated from the relation $\partial/\partial x = U^{-1}\partial/\partial t$. A right-handed Cartesian co-ordinate system is used with x positive in the direction of the mean motion in the boundary layer and z vertically upwards. The fluctuating and mean velocity components are chosen to be u, v, w and U, 0, 0 for the x, y, z directions respectively.

Spectral analysis. The turbulence data were analysed digitally. To prevent significant aliasing, the signals were first passed through low-pass linear-phase-shift filters. Then, after digitizing, a 'fast Fourier transform' algorithm was employed to produce the complex Fourier coefficients of the data and, from these, the power spectrum, coherence and phase. The following notation is used: $\Pi(n)$ for pressure spectral density $[(\mathrm{dyn\,cm^{-2}})^2\,\mathrm{Hz^{-1}}]$ and $\Phi_{ij}(n)$ for velocity spectral and cross-spectral density $[(\mathrm{cm\,s^{-1}})^2\,\mathrm{Hz^{-1}}]$. In most cases these values are given for half-octave bandwidths. Definitions are essentially equivalent to those given by Blackman & Tukey (1959, pp. 167–178), except that the coherence between signals 1 and 2 is

$$\left(\frac{C_{12}^2(n)+Q_{12}^2(n)}{\Phi_{11}(n)\,\Phi_{22}(n)}\right)^{\frac{1}{2}},$$

where C and Q are the co-spectrum and the quadrature spectrum respectively. The data window of this analysis method is the box car type; the results were found to not change significantly if the data were hanned. Time averages are indicated by a bar over the variables, i.e. $\overline{uw}$ or $\overline{p^2}$.

Confidence limits were calculated directly from the data. The total record was broken into a number of shorter data blocks, in which the lowest frequency analysed is the fundamental harmonic of the block. Confidence limits were

calculated by assuming each block to be an independent sample of the data. If the difference between the spectral estimate for each block and the mean over all blocks is assumed to have a Gaussian distribution, then these differences can be used to find the 95 % confidence limits. The assumption is reasonable only if the number of data blocks is quite large, which is true for most runs.

Surface stress. The surface stress was calculated by three different methods: by the eddy flux method using a sonic anemometer, by the 'Φ_{11} method' employing the magnitude of the downstream velocity fluctuations in the inertial subrange (e.g. Weiler & Burling 1967) or, for some of the observations taken over water, by calculation from a drag coefficient, $C_D = 1{\cdot}2 \times 10^{-3}$, related to the mean wind at a height of 5 m. The wind profile was not sufficiently accurate to provide an estimate of surface stress.

3. Results

Approximately 40 separate data 'runs' are specifically involved in presenting the results, and since most of the data are put into a non-dimensional form, the actual operating conditions (surface stress, mean wind, etc.) may not be given explicitly in the main text. Such information is given in tabular form in the appendix. All the data are labelled with a run number (e.g. 120/1) and are listed in numerical order in the appendix.

3.1. *Non-dimensionalizing pressure spectra*

Since the pressure fluctuation is closely related to the velocity fluctuations and is not an independent variable (e.g. Townsend 1955) and since the velocity spectra are readily non-dimensionalized to form the so called 'universal curves', it might be expected that the pressure spectra could equally and as readily be grouped to some universal curve. Such was not found to be the case with the present data. The data include observations from a variety of heights ranging between the surface and 6 m and for a variety of wind speeds and surface roughness, and therefore surface stress, where typical values were between 0·1 and 1 dyn cm^{-2}.

The effect of height on the spectrum was obtained from a group of runs for which two instruments were operating simultaneously at different heights. Examples of the spectra $\Pi(n)$ from measurements with 0, 1·8, 3·75 and 5·5 m vertical separation are shown in figure 4. As can be seen, the spectral intensity at a given frequency exhibits little dependence on z, the height of observation, even at the frequencies where the two signals are essentially incoherent (e.g. coherence $< 0{\cdot}1$ for $n > 0{\cdot}3$ Hz at separation $\Delta z = 5{\cdot}5$ m). This is in direct contrast to velocity spectral intensities, which vary directly as z. All other data collected showed a similar behaviour. The dashed line on the low frequency end of each example is intended to indicate the vertical shift of each pair of curves of spectral estimates. This shifting was done so that more than one pair of curves could be plotted using the same axes. The true magnitude of the lowest frequency pair of points is the value at the intersection of the dashed line with the ordinate.

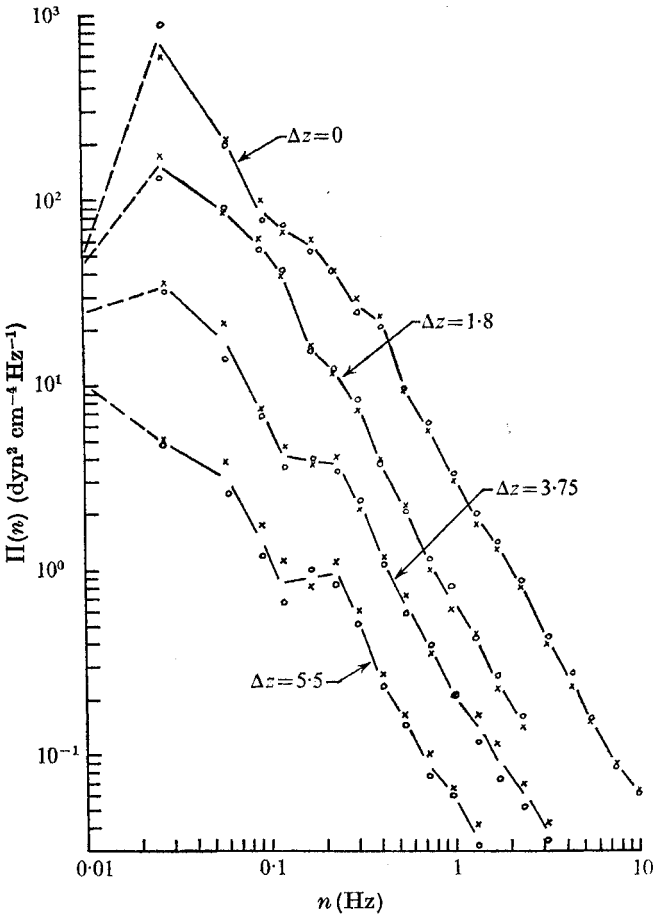

FIGURE 4. Comparison of pressure spectra measured simultaneously at two different heights. Δz is the difference in height, given in metres. ○, upper sensor (at a height z_0); ×, lower sensor (at a height z_x).

Δz (m)	Run	z_x (m)	z_0 (m)
0	165/2	2·5	2·5
1·8	73/2	1·7	3·5
3·75	73/3	1·0	4·75
5·5	186/5	1·25	6·75

It was found that all the data could be grouped in the form shown in figures 5(*a*) and (*b*), plots of $n\Pi(n)\rho^{-2}u_*^{-4}$ against $k_p = \omega U_5^{-1}$, where ρ is the air density and U_5 is the mean wind at 5 m. Vertical lines indicate the 95% confidence limits of the individual estimates. All other data (not shown) were similar but scattered over a wider range than that shown in figure 5. The values of $n\Pi(n)\rho^{-2}u_*^{-4}$ at $k_p = 10^{-2}$ cm^{-1} are plotted in figure 6 as a function of z to demonstrate the scatter. The mean value for the 62 different spectra is about $3{\cdot}5 \pm 0{\cdot}8$. The range of u_*^4 encountered is about $1 \times 10^4 - 50 \times 10^4$ cm^4 s^{-4}. That is, by grouping the data in this way, extreme values of $n\Pi(n)\rho^{-2}u_*^{-4}$ at a given k_p now differ by a factor of 2 whereas the extremes of the dimensional spectral $n\Pi(n)$ differed

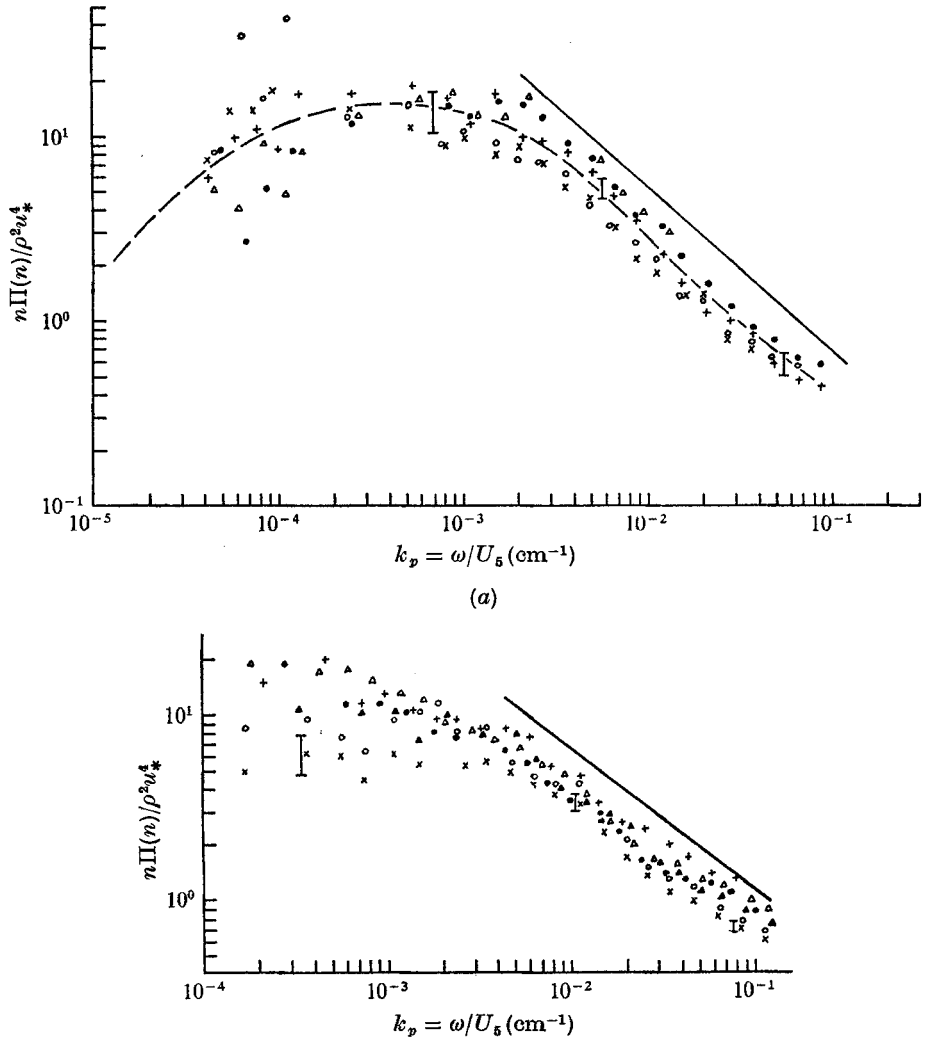

FIGURE 5. Pressure spectra plotted as $n\Pi(n)\rho^{-2}u_*^{-4}$ against ω/U_5. (*a*) Over water. ×, run 110/1; ○, run 110/2; ●, run 120/1; +, run 120/2; △, run 121/1; I, 95 % confidence limits. Slope of solid line is −0·7. (*b*) Over land. ×, run 319/1; ○, run 319/2; △, run 320/1; +, run 320/2; ●, run 425/1; ▲, run 425/2; I, 95 % confidence limits. Slope of the solid line is −0·7.

by a factor of about 50. The scatter between spectra, shown in figure 6, could not be improved with the present data since u_*^2 is known at best to within ± 20 %, and therefore $\rho^2u_*^4$ only to about ± 40 %. Most of the values of $n\Pi(n)\rho^{-2}u_*^{-4}$ shown in figure 6 are within this range; therefore the scatter might be due entirely to the error in u_*^2 rather than to dependence on some other variable. The data shown in figure 5 are not 'universal' in that the abscissa has dimensions of (length)$^{-1}$. A parameter that could be used to non-dimensionalize k_p but be independent of the height of observation is z_0, the surface roughness. However,

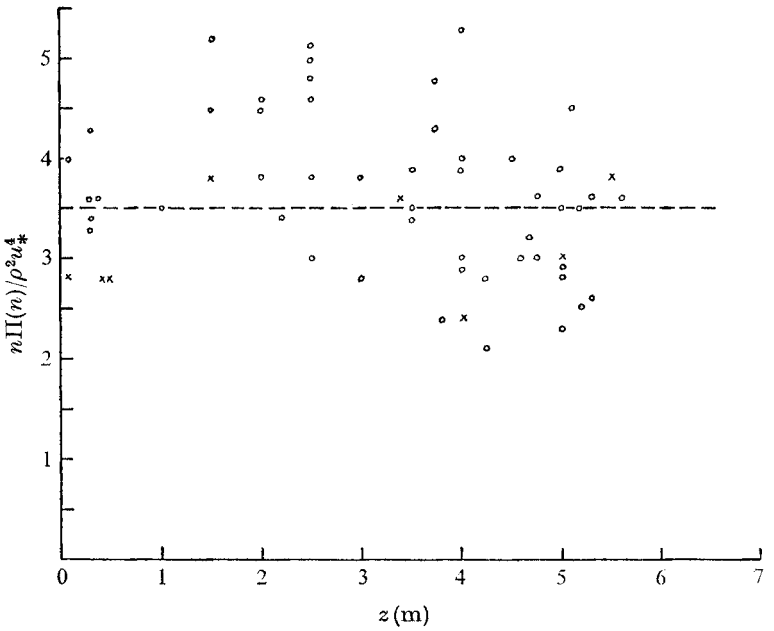

FIGURE 6. Summary of pressure spectra plotted as in figure 5. Points shown are for $n\Pi(n)\rho^{-2}u_*^{-4}$ at $\omega/U^5 = 10^{-2}\,\mathrm{cm}^{-1}$. z is the height of observation. ×, using the sonic to evaluate the stress; ○, using C_D or the Φ_{11} method.

a plot of $n\Pi(n)\rho^{-2}u_*^{-4}$ versus $k_p z_0$ does not group the data as well as the above method (z_0 was evaluated from a drag coefficient and differed by a factor of 10 between the two sites).

There has been reasonable success in scaling wind-tunnel wall pressure data using the basic parameters of the flow. For example, Blake (1970) was able to group data for both a rough and a smooth wall. In addition to the stress and surface roughness as scaling variables, he used both a boundary-layer thickness and free-stream velocity. Unfortunately, these latter two variables are generally unknown and difficult to define for the atmosphere. As a result, no direct comparison with published wind tunnel data is possible. Another method for grouping the atmospheric data is illustrated in figure 7, a plot of $\Pi(n)\nu^{-1}\rho^{-2}u_*^{-2}$ versus $\omega\nu u_*^{-2}$, where ν is the kinematic viscosity of air. Though this method is difficult to justify physically, a direct comparison with wind tunnel data would be possible. The scatter between spectra is about the same as with the previous method; the mean value of $\Pi(n)\nu^{-1}\rho^{-2}u_*^{-2}$ at $\omega\nu u_*^{-2} = 10^{-4}$ is $(4 \pm 1) \times 10^5$.

One other parameter that might have influenced the data shown above is the stability. As estimated by the Richardson number, most of the data were collected under conditions of nearly neutral local stability (see appendix). The stability was not measured at the Ladner site, however, the observations were taken there on cloudy (but dry) days when local buoyancy effects would be at a minimum. Recent work (McBean 1971) shows that the non-dimensionalizing of velocity is relatively insensitive to stability over the range of values measured in this study. Even though the stability near the surface was almost neutral it is possible that

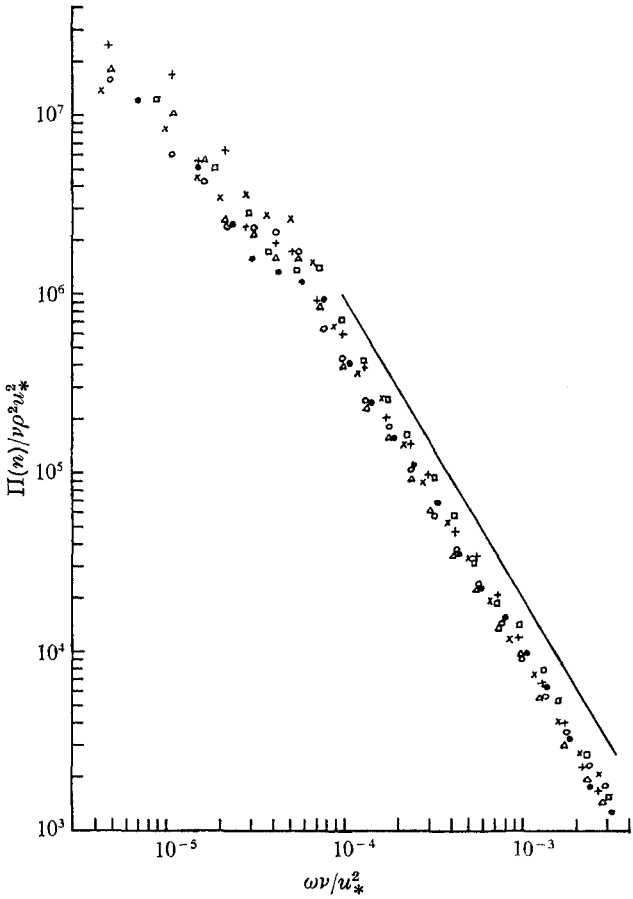

FIGURE 7. Pressure spectra from measurements over water plotted as $\Pi(n)\nu^{-1}\rho^{-2}u_*^{-2}$ against $\omega\nu u_*^{-2}$. Slope of solid line is $-1{\cdot}7$. ×, run 73/1; ○, run 141/2/1; △, run 141/3; +, run 141/2/2; ●, run 72/1; □, run 72/2.

the stability at higher elevations may have affected the low frequency portions of some of the pressure spectra.

The data given by Gorshkov (1967) do not seem to agree with these present results; they do not exhibit the u_*^4 dependence shown here. As the wind speed increased, the intensity of his pressure spectra did not necessarily increase. However, it is not indicated in his paper whether all his measurements were taken with a nearly constant surface roughness.

3.2. *Shape and intensity of the spectrum*

The mean shape of the pressure spectra in figure 5 is compared in figure 8 with previously published atmospheric data. The mean curves for the present data and for Priestley's are normalized, the others are arbitrarily shifted vertically to lie near the mean curve from figure 5. All these spectra are from observations at comparable wind speeds. As shown by figure 8, the power law for the pressure

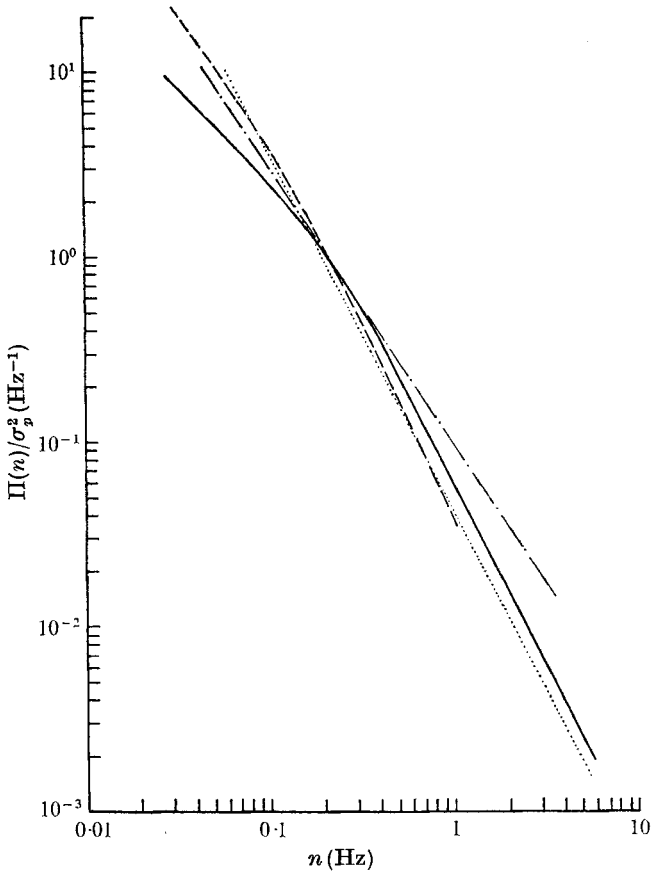

FIGURE 8. Comparison of the average spectral slope of pressure spectra obtained in the atmospheric boundary layer by various authors. ——, present work, figure 5; – –, Priestley; –·–, Gossard; ····, Gorshkov.

spectra in the present study is similar to that obtained by other authors using different instrumentation at different sites. Thus, except for some of the differences at the low frequencies, which may be due to contamination by mesoscale sources in some data, there appears to be a power law 'typical' for atmospheric data.

A discussion of how this 'typical' spectrum relates to the scales of the boundary layer can best be done by comparison with the better known and more familiar velocity spectra. Velocity fluctuations were measured with a sonic anemometer at the same time and height as were the pressure fluctuations, whose spectra are shown in figure 5(*a*). The velocity spectra, figure 9, conform to the 'universal curves' obtained by McBean (1971). At values of $f = nz/U > 1$, i.e. at non-dimensional frequencies larger than at the peak of the w spectrum, the velocity spectra follow with a reasonable fit the $-\frac{2}{3}$ slope predicted by dimensional arguments for an inertial subrange; the straight line (figure 9) has this predicted slope. The corresponding range for the pressure spectra, figures 5 and 7, is approximately $k_p > 3 \times 10^{-3}$ or $\omega\nu/u_*^2 > 7 \times 10^{-5}$. This is the range in

which the pressure spectra have a well-defined power law with $k\Pi(k) \propto k^{-0.7}$ (approximately).

Dimensional arguments identical to those used to predict a $-\frac{2}{3}$ region for the velocity spectrum through the inertial subrange have been used by Obukhov to predict the shape of the pressure spectrum, $\Pi(k)$ (Lumley & Panofsky 1964, p. 84). For this restricted scale range with no production and no dissipation, he obtained

$$k\Pi(k) \propto k^{-\frac{4}{3}}. \tag{1}$$

Although individual spectra show some variation from the mean slope, all are significantly different from the $-\frac{4}{3}$ predicted. It is apparent that the flow must be sufficiently anisotropic at these scales (see Stewart 1969) such that the pressure spectra do not agree with the inertial subrange prediction even though the velocity spectra do agree reasonably well. The scales of the turbulence at frequencies near $f = 1$ are of the order of 50 cm, sufficiently large that an interaction with mean shear would be expected.

At the larger scales, i.e. $k_p < 3 \times 10^{-3}$ in figure 5, the pressure spectra do not show any definite power-law behaviour but simply decrease in slope in a manner similar to that seen in velocity spectra, and usually reverse slope, see figure 5(*a*). There appears to be no strong influence from low frequency contamination by mesoscale phenomena such as was found in pressure spectra by Gossard (1960). Because of the short length of the data runs the analysis could not be continued to a lower frequency than those shown.

A theoretical argument based on similarity assumptions, see Bradshaw (1967), predicts that $\Pi(k) \propto k^{-1}$ (or $k\Pi(k) =$ constant) for the spectrum of the fluctuations in surface pressure. There is some support for this law in the wind tunnel data of Bull (1967) and Blake (1970). Although the atmospheric data (figure 5(*a*) and (*b*)) go through a zero slope, they do not contain any significant range of scales where the slope is constant near a value of zero.

The data given in figure 5 were used to evaluate the relationship between the pressure variance and the surface stress assuming that the pressure fluctuations are entirely due to the boundary-layer turbulence. The dashed line among the data of figure 5(*a*) was replotted on a log–linear scale and integrated with respect to $\log k_p$ from a wavenumber $k_p = \omega/U_5$ of 10^{-5} to 2×10^{-2} cm^{-1}. The integration gives the root-mean-square pressure in terms of the surface stress ρu_*^2:

$$(\overline{p^2})^{\frac{1}{2}} = 2{\cdot}6\rho u_*^2. \tag{2}$$

This relation is almost identical to that obtained from surface measurements in wind tunnels (Willmarth & Wooldridge 1962). Since, as shown above, the curve integrated to obtain the root-mean-square pressure is not a function of height, the relationship would be expected to hold at the surface. The magnitude given by equation (2) is also in the range predicted theoretically by Kraichnan (1956).

A more detailed comparison between the pressure and the velocity is shown in figure 10. Two curves representing the variance within narrow frequency bands of the non-dimensional pressure and of the non-dimensional sum of the three velocity components from run 120/1 are plotted against frequency. The values plotted are $(\Pi(n)\,\Delta n)^{\frac{1}{2}}/\rho u_*^2$ and $(\Phi_{11} + \Phi_{22} + \Phi_{33})\,\Delta n/u_*^2$, where Δn is the band-

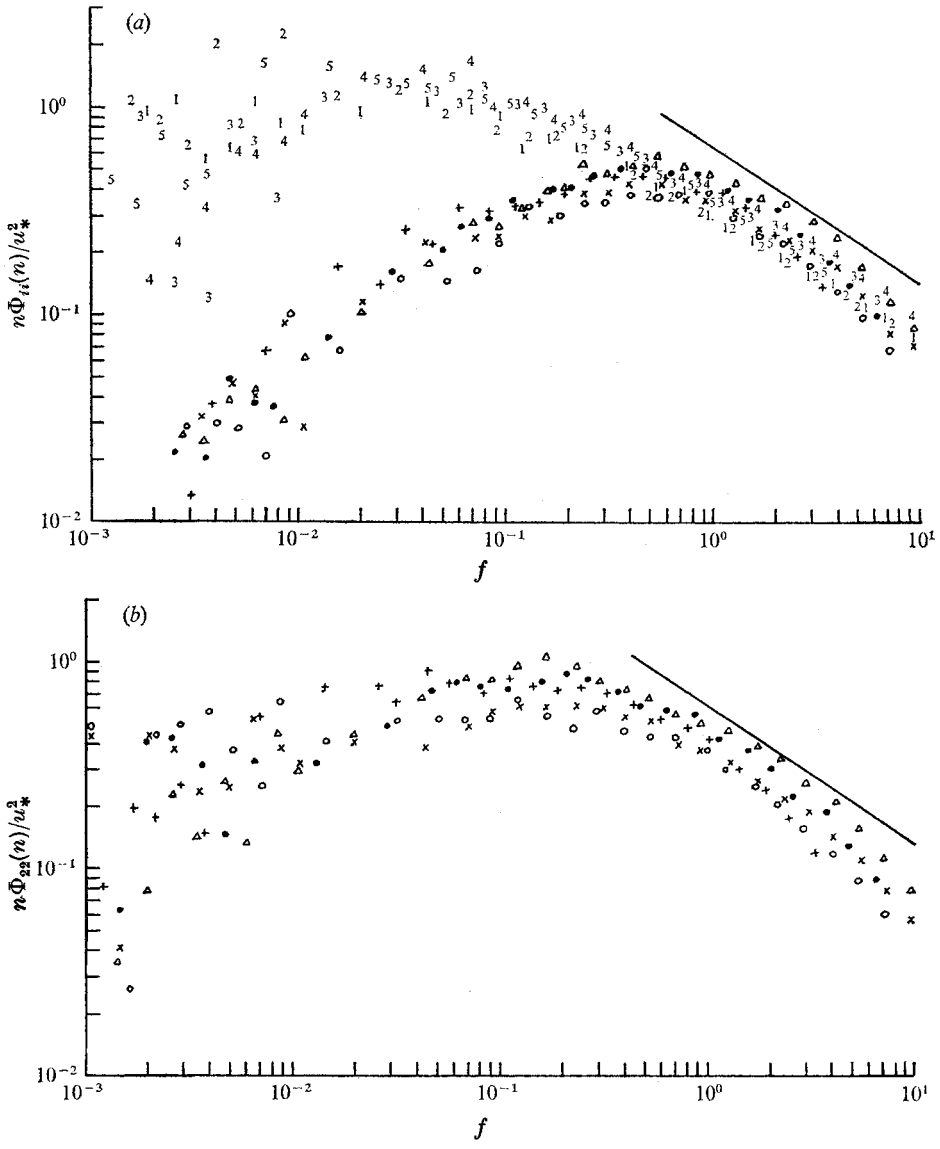

FIGURE 9. For legend see facing page.

width. The velocity components and the stress were measured using a sonic anemometer at the same level as the pressure probe. The values have been plotted in this form to show how the relationship between the pressure variance and velocity variance changes for different scale ranges. As can be seen, both curves exhibit a similar shape; peaks in the pressure curve correspond to peaks in the velocity curve. This comparison is dependent on the bandwidth chosen since the pressure curve and the velocity curve vary as $(\Delta n)^{\frac{1}{2}}$ and Δn respectively. Also, since the velocity curve is a function of z and the pressure curve is not, this relationship has some z dependence, which is most noticeable at the high frequencies, near and above the peak of the w spectrum. However, the positions of

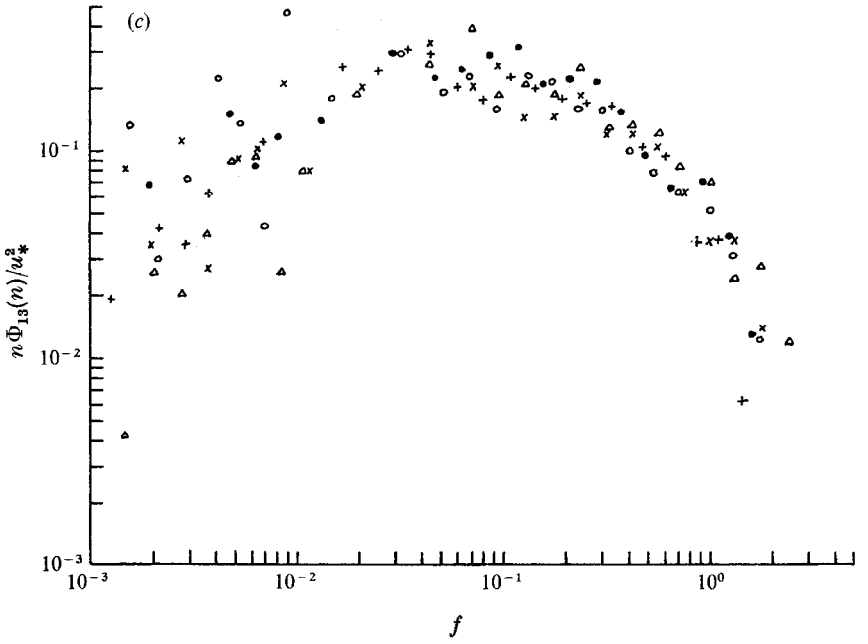

FIGURE 9. Non-dimensionalized velocity spectra, $f = nz/U$. (*a*) u and w spectra. Numbers refer to u spectra, symbols to w spectra. 1, ×, run 110/1; 2, ○, run 110/2; 3, ●, run 120/1; 4, △, run 120/2; 5, +, run 121/1. (*b*) v spectra. ×, run 110/1; ○, run 110/2; ●, run 120/1; △, run 120/2; +, run 121/1. (*c*) $\overline{uw}$ spectra. ×, run 110/1; ○, run 110/2; ●, run 120/1; △, run 120/2; +, run 121/1.

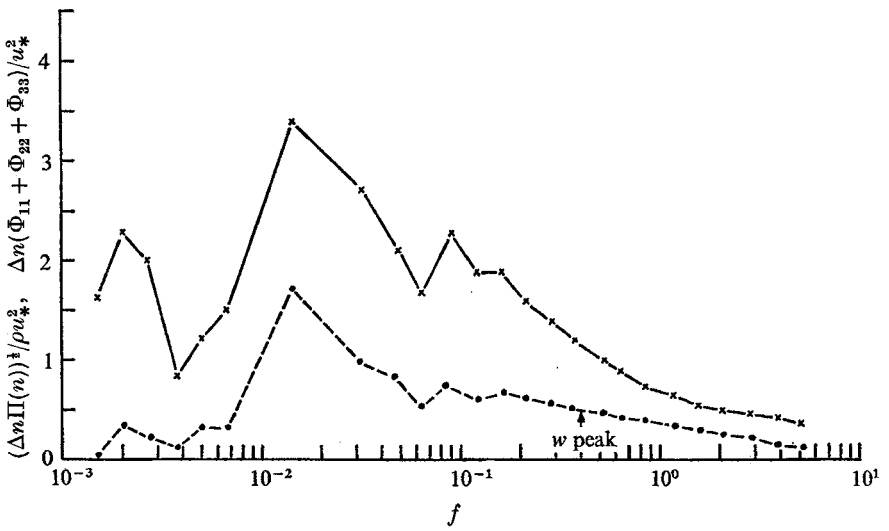

FIGURE 10. Comparison between a non-dimensionalized variance of the pressure and of the velocity components for run 120/1 for different frequency bands. —×—, $(\overline{p^2})^{\frac{1}{2}}/\rho u_*^2$; – –●– –, $(\overline{u^2}+\overline{v^2}+\overline{w^2}/u_*^2)$.

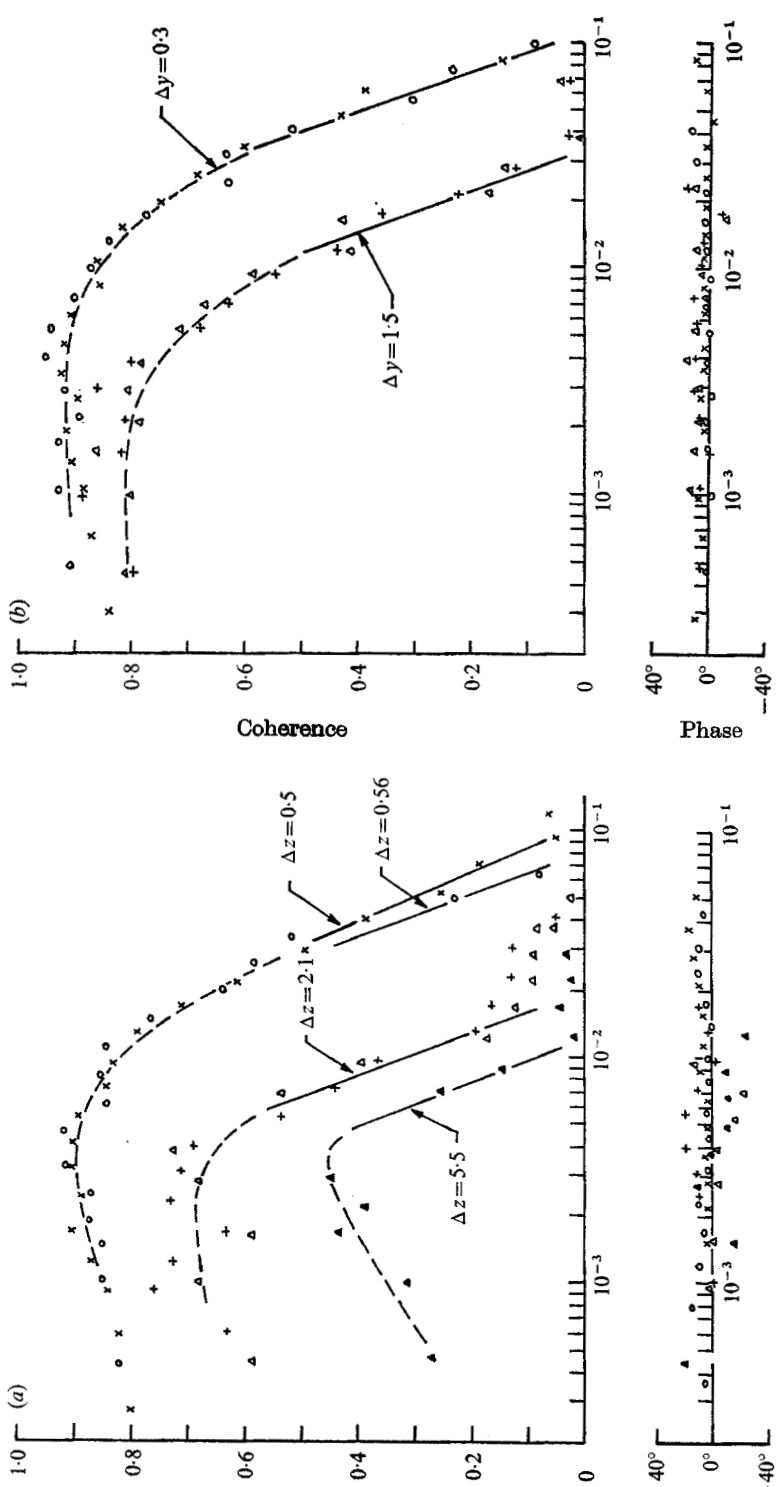

FIGURE 11. Coherence and phase between two pressure measurements at separate stations. (*a*) With various vertical separations Δz (m). Phase positive means p upper leads p lower. ×, run 173/2; ○, run 200/2; +, run 173/1; △, run 186/4; ▲, run 186/5. (*b*) With various cross-stream separations Δy (m). ×, run 172/2; ○, run 186/3; +, run 205/1; △, run 205/2. (*c*) With various downstream separations D (m). Δz for all runs is 30 cm. ×, run 319/1; ○, run 319/2; △, run 320/1; +, run 320/2; ●, run 425/1; ▽, run 426/1. The inset on the phase plot is to show the phase change on a linear frequency axis.

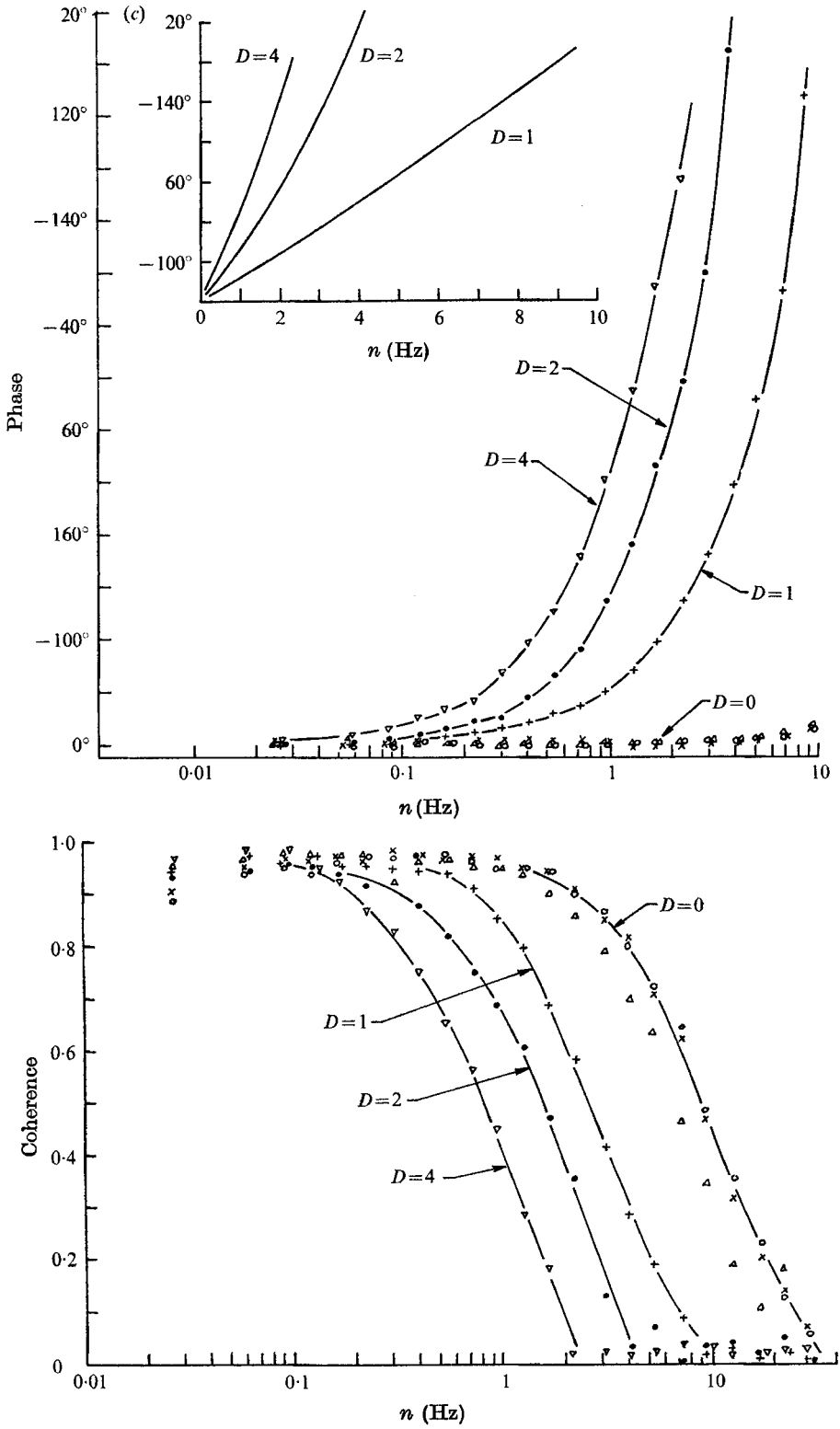

FIGURE 11(*c*). For legend see facing page.

spectral maxima and minima have neither a strong z dependence, since they arise from low frequency u and v fluctuations of scales much larger than the observation height, nor a strong bandwidth dependence. The general property of peaks in the velocity curve corresponding to peaks in the pressure curve were present in all other data.

3.3. *Some kinematics of the pressure fluctuations*

Some properties of the structure of the fluctuations in static pressure can be deduced from the simultaneous measurement of the pressure at two points. By examining the relative phase and coherence between observations spaced in each of the three principal directions, the orientation, a scale size and a propagation velocity of the fluctuations were evaluated.

The coherence and phase between the pressure at two points with vertical (Δz) and transverse (Δy) separations are shown in figures 11 (*a*) and (*b*). The phases plotted are for frequencies at which the coherence is greater than 0·2. The separations used are sufficiently large to observe any phase shifts that may be present in the pressure fluctuations for scales of about 0·5–5 m. For vertical separations of up to 5 m the average phase difference is near zero. Thus there is no preferred vertical orientation for the pressure fluctuation in this range. As expected, the average relative phase for transverse separations is not significantly non-zero.

Examples of the coherence and phase for two sensors with a downstream separation are shown in figure 11 (*c*). In most cases these data are from a surface sampling port upwind and a downwind sensor 30–50 cm above the surface (the arrangement used is that described in § 2.2). Ideally, to conform with the 'frozen field hypothesis' the coherence should be one at all frequencies for all downstream separations and a phase difference should result, its size depending on the downstream separation of the pressure sensors. Figure 11 (*c*) shows that the signals become essentially incoherent for phase shifts of about 360° or after propagating approximately one wavelength.

From the coherence between two pressure signals at a given separation, a scale for the pressure fluctuations can be determined. When measuring the pressure with two pressure sensors at a fixed separation perpendicular to the mean flow, pressure fluctuations with a 'scale' size large compared with the separation of the sensors will often occur simultaneously in the two signals, producing a high coherence, while fluctuations with a 'scale' size small compared with the separation cannot occur simultaneously. Those fluctuations with a 'scale' comparable to the probe separation can occasionally produce some coherent signal at the two probes. The pressure scale length at frequency n_1, $L_p(n_1)$, is defined as that separation at which the coherence falls through some low but measurable value. Though this is an arbitrary definition it does provide a realistic measure of scale size, found to be useful in interpreting some of the data. The scale chosen is that at which

$$\Pi_{12} \simeq (1/e^2)\,\Pi_1 \simeq (1/e^2)\,\Pi_2,$$

where Π_{12} represents the coherent energy between two signals of energy Π_1 and Π_2, and $e = 2{\cdot}72$. In other words, where

$$\text{Coherence} = (\Pi_{12}^2/\Pi_1\Pi_2)^{\frac{1}{2}} = 1/e^2 = 0{\cdot}14.$$

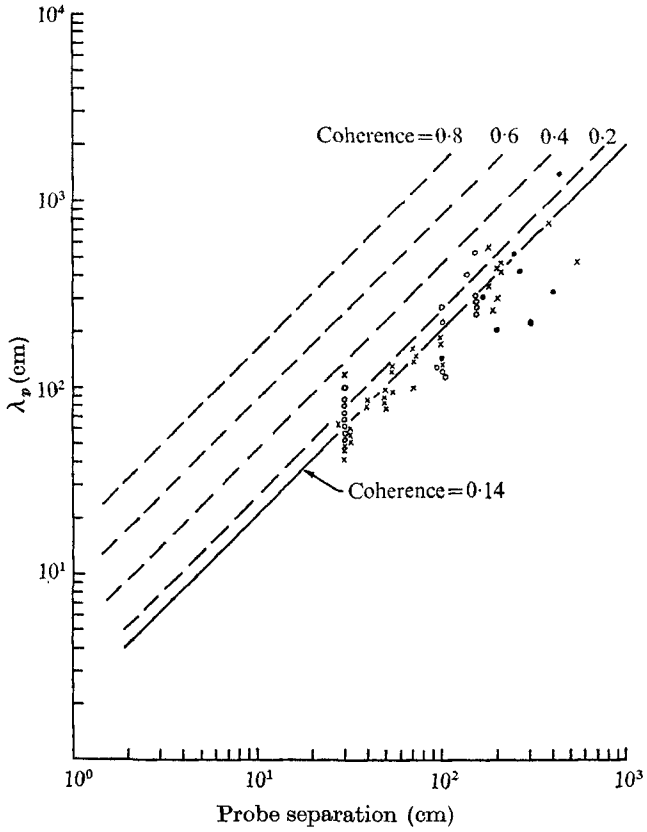

FIGURE 12. A comparison between the scale length λ_p ($= U/n$) and the probe separation when the coherence between two pressure measurements has dropped to 0·14. ●, $\lambda_p(x)$; ○, $\lambda_p(y)$; ×, $\lambda_p(z)$.

(For separations perpendicular to the mean flow a scale based on the coherence is equivalent to a scale based on the correlation coefficient.) The scale lengths evaluated in this manner are then compared with the downstream wavelength $\lambda_p(n_1)$, calculated from the 'frozen field' hypothesis. For the calculations it is assumed that the propagation velocity of the pressure fluctuations, U_p, is approximately equal to the wind at 5 m, U_5. It will be shown later that for data analysed in this manner this is a reasonable approximation. Then $\lambda_p(n_1) \simeq U_5/n_1$. Probe separations (equivalent to L_p for $n = n_1$) are plotted as points against λ_p for coherences of 0·14 on a log–log plot in figure 12. The solid line drawn among the points has a slope of 1, that is, L_p varies directly as λ_p. The plot shows that probe separations in all directions yielded similar L_p for a given λ_p (including the downstream separation). Thus, as a first approximation, the mean shape of a pressure fluctuation is equiscalar. Wind tunnel observations (Willmarth & Wooldridge 1962) agree with the result that the horizontal scales are comparable in size. For the definition of scale used, an L_p of 100 cm, for example, corresponds to a λ_p of 210 cm. Therefore the actual size of pressure fluctuations (L_p) is approximately one-half of a wavelength λ_p.

Site	L	L	L	L	BB	BB	SB	SB	SB
Run	320/2	425/1	425/2	426/1	137/2	142/1	196/1	196/2	196/3
U_5 (m s^{-1})	7·7	6·1	5·2	6·1	4·1	4·3	3·7	3·4	3·7
D (m)	0·96	2·0	3·1	4·1	0·56	0·56	4·3	2·7	1·5
U_p/U_L	0·90	0·97	1·49	1·08	0·96	0·95	1·20	1·15	1·10
	0·91	0·93	1·17	1·04	0·99	0·99	1·30	1·15	1·00
	0·96	0·91	1·04	0·99	1·10	1·05	1·10	1·14	1·05
	1·00	0·86	0·98	0·93	1·30	1·20	1·05	1·10	—
Average U_p/U_L	0·94	0·92	1·17	1·01	1·07	1·05	1·16	1·14	1·05

TABLE 1. Pressure propagation velocity U_p as a fraction of U_L

The family of curves of constant coherence in figure 12 has been added for convenience and will be used later when we consider the influence of probe separation on data. The separation between lines of constant coherence is taken from the roughly linear fall-off of coherence shown in figure 11; this fall-off is approximately the same for all cases, having a slope of about $-0{\cdot}7$.

The above results on scale size can be used to estimate the expected 'decay rate' of the pressure fluctuation. Assuming that the pressure fluctuations result from the complete acceleration or deceleration of a velocity fluctuation, the order of magnitude of $[(1/\rho)\,(\Delta p/\Delta X_i)]$ will be of the order of $\Delta u_i/\Delta t$, where Δ indicates the r.m.s. fluctuations from the mean. For run 120/1 (figures 5 and 9) at 0·7 Hz (bandwidth = 0·21 Hz), $w \simeq u \simeq v \simeq 10\,\mathrm{cm\,s^{-1}}$, $\Delta p \simeq 1\,\mathrm{dyn\,cm^{-2}}$. The gradient of p will act over a distance of about $\frac{1}{2}L_p$. Thus, for example,

$$\Delta X_i = \tfrac{1}{2}L_p = U_5/4n_1 \simeq 250\,\mathrm{cm}.$$

These values give $\Delta t = \rho \Delta u\, \Delta x/\Delta p \simeq 3$ s. A comparable Δt of about 4 s is obtained if the 'decay time' is assumed to be the time required for a pressure fluctuation to travel about three wavelengths. This is similar to the results obtained in a wind tunnel by Willmarth & Wooldridge (1962), who found, using time lag covariances, that significant energy had been lost by a pressure pattern that had travelled a distance of about two to three wavelengths (see their figure 10).

The phase difference between two simultaneous pressure measurements with a downwind separation can be used to evaluate a mean propagation velocity of the pressure fluctuations. Figure 11 (*c*) shows the phase difference θ for downwind separations D of about 0, 1, 2 and 4 m. The measurement upwind was of surface pressure and that downwind was in the air at a height of 32 cm. The propagation velocity is calculated from

$$U_p = (1/\theta)\, D n_\theta \times 360^\circ, \tag{3}$$

where n_θ is the frequency at which the phase difference is θ. The velocity U_p is then compared with the mean wind U_L at the height L_p appropriate to the frequency n_θ, since this height is more representative of the mean wind at the 'centre of gravity' of the pressure fluctuations of frequency n_θ. The mean wind at level L_p is interpolated from observed cup profiles. Table 1 gives the results of the velocity comparison. Four different phase differences were used: 90°, 180°,

270° and 360°. Since the scale size L_p is different for each phase difference, the U_L used for comparison with U_p is evaluated for each phase shift. The Ladner observations (L), considered to be the most accurate because of low instrument noise and steady mean flow, give values (from 4 runs) of $1{\cdot}0 \pm 0{\cdot}1$ for U_p/U_L. Similar observations at Spanish Banks (SB) give (from 3 runs) $1{\cdot}1 \pm 0{\cdot}15$ and at Boundary Bay (BB) (from 2 runs), $1{\cdot}05 \pm 0{\cdot}1$. Thus the pressure field travels at about the 'local' mean wind speed, the higher frequencies or smaller scales travelling more slowly than the lower frequencies or larger scales. Calculations by other investigators working in wind tunnels (see Willmarth & Wooldridge 1962) give an asymptotic value of about $0{\cdot}8U_\infty$ for the propagation velocity. This difference is considered to be due to the choice for the mean wind used for the comparison. The value of U_∞ for the atmospheric boundary layer could easily be 15–20 % higher than the wind at height L_p, which would account for the difference. The observation that the propagation velocity is a function of frequency (or scale size) has also been observed in wind tunnels.

If the height L_p is calculated by taking $U_5/2n_\theta = L'_p$ as a first approximation and then letting $L_p = U_L/2n_\theta$, the second step adds a correction of less than 10 %. Thus the assumption of $U_p \simeq U_5$ in evaluating the λ_p of figure 12 was accurate to within about 10 %.

A similar analysis was done on some velocity measurements to provide a comparison with the pressure. The data came partly from observations taken by other workers at the Institute of Oceanography, University of British Columbia, using sonic and hot-wire anemometers over water, and partly from hot-wire anemometer observations at the Ladner site. Coherences for all velocity components fell off approximately as $\log(n)^{-0{\cdot}8}$, which is about the same as for the pressure field. A scale L_v defined in the same way as L_p gives the size of the velocity fluctuations as approximately one third of the wavelength $\lambda_v = U/n_L$. Velocities are also roughly equiscalar and in phase at points separated vertically and across the stream. The propagation velocity is about U, as expected. These results indicate that the pressure and velocity fluctuations are similar in geometry and are advected at the same rate.

3.4. *Pressure–velocity relationships*

In this section a number of pressure measurements and simultaneous velocity measurements are used to establish some of the pressure–velocity relationships in the scale range for which there is an active Reynolds stress. *A priori*, there was no specific relationship expected. Kraichnan (1956) has shown theoretically that for non-isotropic turbulent boundary-layer flow, the type of flow in which the present measurements were taken, the primary contribution to pressure fluctuations near the surface results from interaction between the turbulence and the mean shear. Also, pressure fluctuations are credited with being the 'isotropy producing' force; that is, they are expected to transfer energy among velocity components in such a way as to build up the weaker component at the expense of the stronger (e.g Batchelor 1960, p. 88). If pressure is doing work across a plane, then the velocity component normal to the plane and in the direction

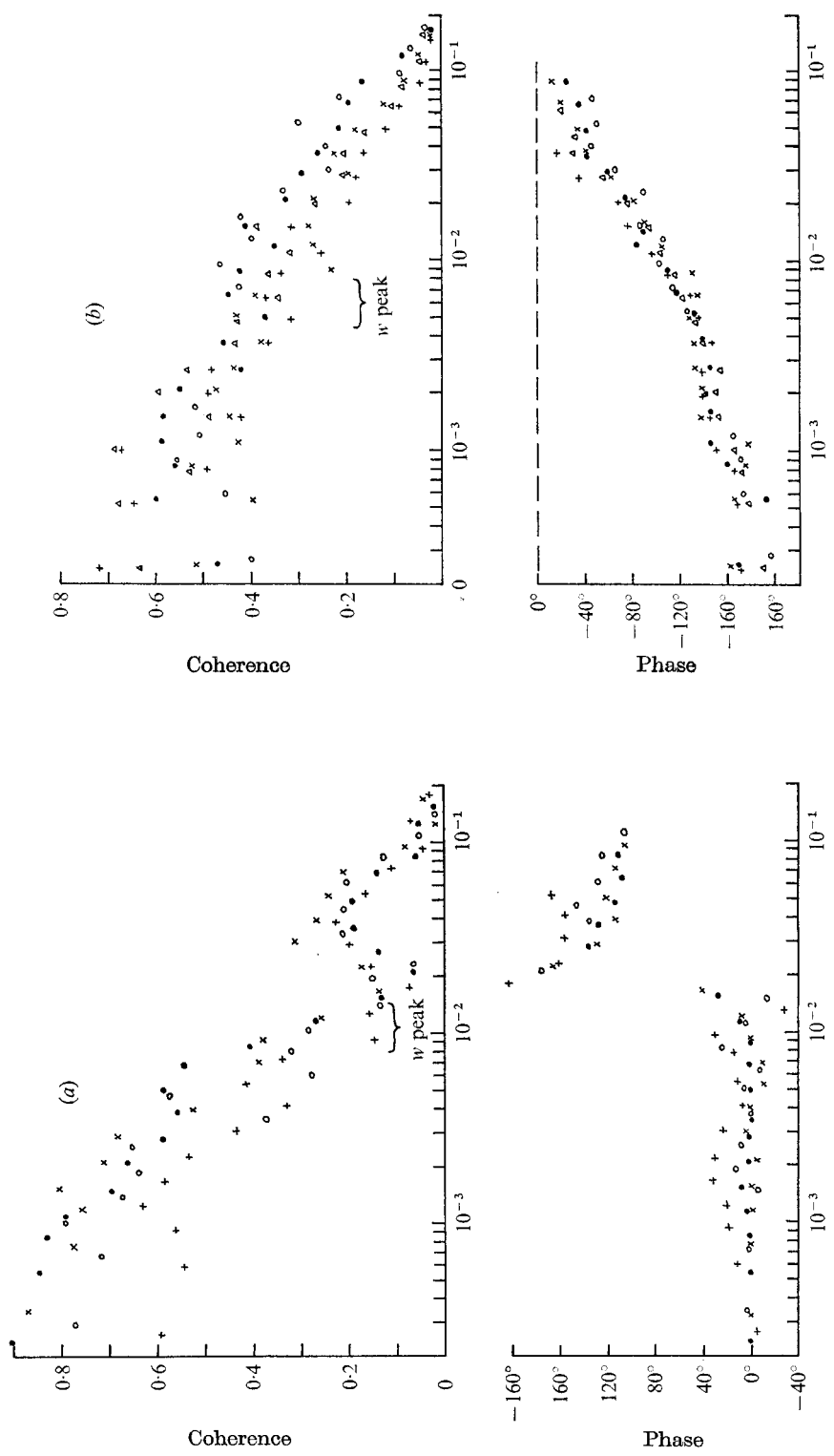

FIGURE 13. Coherence and phase between pressure and velocity components. $k = w/U$. (*a*) Between p and u, u being measured with a hot wire. Height of observations ranged from 1·5 to 3 m. Phase positive means p leads u. ×, run 172/1; ○, run 172/2; +, run 173/1; ●, run 173/2. (*b*) Between p and w, w being measured with sonic anemometer. Height of observations ranged from 1·5 to 5·5 m. Phase positive means p leads w. ×, run 120/2; ○, run 121/1; +, run 110/1; △, run 110/2; ●, run 120/1.

towards the fluid receiving energy would on the average be in phase with the pressure.

Typical measured coherence and phase relationships between p and the velocities u and w are plotted in figures 13 (a) and (b). Positive phases labelled p–u, p–w, etc., mean that p leads u, w, etc., respectively. Data in figure 13 (a) were obtained from the pressure probe and a hot wire, 4 cm to the side of and 5 cm behind the probe. The data are representative of at least ten other runs. Figure 13 (b) uses data from the sonic, with the pressure probe placed about 25 cm upwind of the centre of the sonic paths; this positioning of the probe was checked in a wind tunnel to ensure that no significant dynamic pressure noise would be present. The pressure signal was corrected for its spatial phase lead using Taylor's hypothesis. The approximate peak of the w spectrum (at $f = nz/U \simeq 4 \times 10^{-1}$, see figure 9) is marked by an arrow for ease of comparison with standard velocity spectra. These plots show that the pressure is 'in phase' with u at low frequencies; (the opposite of Bernoulli type and the opposite of that expected from dynamic noise from the probe) with coherences up to 0·8, while at high frequencies the phase difference becomes about 135° (indicating that some energy transfer was taking place) with coherences of about 0·1–0·2. The phase transition, that is, the change between the 'in phase' situation and the 'large phase difference' is associated with a loss of coherence in $\overline{pu}$. It occurs at a frequency somewhat higher than that at the peak of the w spectrum, near the highest frequencies of significant $\overline{uw}$ (see figure 9). The coherence in the $\overline{pw}$ relationship, in contrast, shows a gradual decrease from about 0·5 at low frequencies to near zero at high frequencies; the corresponding phase change is gradual from about 180° to near zero. Some of the loss of coherence in the $\overline{pw}$ relationship at the highest frequencies may be due to probe separation (see figure 12). As would be expected the measured $\overline{pv}$ coherence (not shown) is near zero for the same frequency range.

A reason for the well-defined change in the p–u phase can be seen from a plot, figure 14, of the wavelength λ_p at this transition, as a function of z (height of observations above the surface). The wavelength is calculated using the first data point *after* the phase transition to near 135°. Also shown is a dashed line indicating the scale size L_p of the pressure fluctuations for the transition frequency ($L_p \simeq \frac{1}{2}\lambda_p$ as evaluated in the above section). All points fall near or below the line $L_p = z$. That is, all pressure fluctuations with a downstream scale size larger than z have a different phase relationship from those with scale size less than z. Since the pressure fluctuations are approximately equiscalar (see § 3.3) this effect can be attributed to the larger scale fluctuations, those whose vertical scale is larger than the measurement height, 'feeling' the bottom. A positive pressure will occur near the surface when downward moving air, typically of higher than average u, is decelerated upon contact with the boundary. Similarly, a negative pressure near the surface will result when air is moving upward, away from the surface. Fluctuations with scales smaller than the measurement height have a different relationship since they are not directly influenced at the bottom.

Even though the major source of the low frequency pressure fluctuations is attributed to air motions interacting with the surface, not all w fluctuations

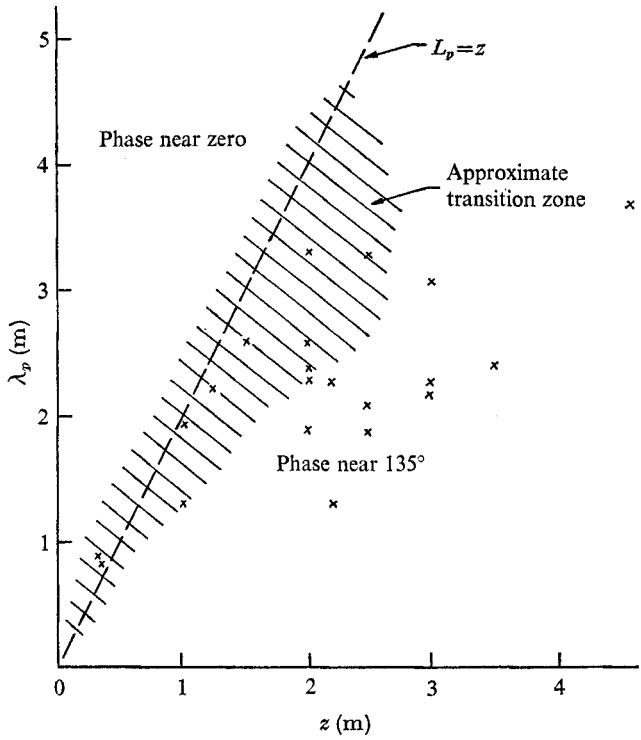

FIGURE 14. Wavelength of the pressure fluctuations associated with the p–u phase transition as a function of observational height. – – –, measured scale size.

produce corresponding pressure fluctuations. The coherence between the pressure and w is lower than between pressure and u at these scales (see figures 13(*a*) and (*b*)). Since it is felt that this is a real effect and not due to the instrumentation, the flow must contain significant w fluctuations which do not produce corresponding u or p fluctuations. As can be seen by comparing figures 15 and 13(*b*), the u–w and p–w coherences are both about 0·5 on these scales.

Evidence that most of the pressure at low frequencies is associated with deceleration of downward motion can be seen from the coherence between velocity and two pressure measurements near the surface (see figure 16). One pressure sensor was at the surface, and a hot-wire anemometer and a pressure probe were together at 30 cm. The surface pressure signal has a higher coherence with downstream velocity fluctuations than does the pressure signal from the pressure measurement in the air. The mean difference in coherence is about 0·1 with the 30 cm separation. The two pressure signals are in phase for frequencies less than 5 Hz, see figure 11(*c*). Since the two pressure signals have the same spectral level and zero phase with respect to the velocity, the difference in coherence is the result of the in-phase pressure at the surface being on the average larger than the in-phase pressure at the level of the velocity sensor. This means that the pressure gradient is on the average directed upward. A calculation, see table 2, shows this for run 319/1.

The coherences between u and p at 30 cm (see figure 16) are significantly

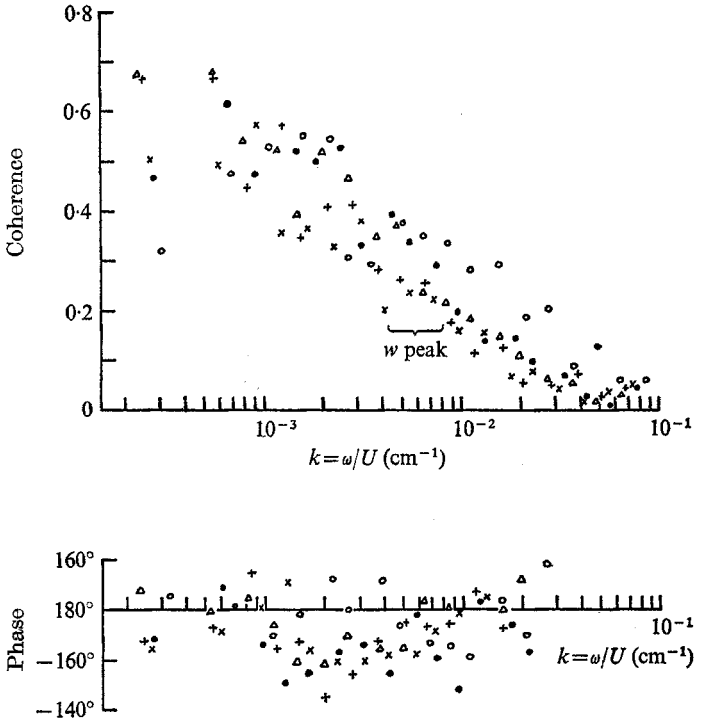

FIGURE 15. Coherence and phase between u and w velocity components, measured with a sonic anemometer. Height of observations ranged from 1·5–5·5 m. Phase positive means that u leads w. ×, run 120/2; ○, run 121/1; △, run 110/2; +, run 110/1; ●, run 120/1.

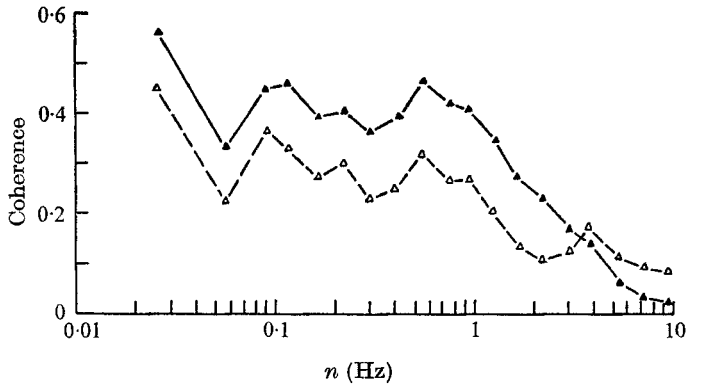

FIGURE 16. Coherence between downstream velocity u and two pressure measurements for run 320/1. △, one pressure sensor beside the u sensor; ▲, one pressure sensor at the surface, 30 cm below.

smaller than those typically measured at higher levels, as shown in figure 13 (*a*). This is thought to be an example of the 'integral effect' operating near the boundary where, for example, some of the downward air motions may be decelerated completely, before reaching the boundary, by a pressure field observed at the boundary; increases in downstream velocity would then occur as a result of the local increase in shear rather than being directly due to vertical advection.

Frequency (Hz)	Bandwidth (Hz)	$\overline{\Delta pu}$†	$(\Phi_u)^{\frac{1}{2}}$ (cm s^{-1} Hz$^{-\frac{1}{2}}$)	Δp‡ (dyn cm^{-2})	$\Delta p/\Delta z$ (dyn cm^{-3})
0·026	$3{\cdot}1\times10^{-2}$	$-6{\cdot}3\times10^{3}$	$4{\cdot}6\times10^{2}$	2·4	$-7{\cdot}7\times10^{-2}$
0·059	$3{\cdot}1\times10^{-2}$	$-4{\cdot}2\times10^{3}$	$3{\cdot}6\times10^{2}$	2·1	$-6{\cdot}8\times10^{-2}$
0·090	$3{\cdot}1\times10^{-2}$	$-2{\cdot}2\times10^{3}$	$3{\cdot}0\times10^{2}$	1·3	$-4{\cdot}2\times10^{-2}$
0·12	$3{\cdot}1\times10^{-2}$	$-1{\cdot}2\times10^{3}$	$2{\cdot}4\times10^{2}$	0·87	$-2{\cdot}9\times10^{-2}$
0·17	$6{\cdot}1\times10^{-2}$	$-6{\cdot}0\times10^{2}$	$1{\cdot}8\times10^{2}$	0·81	$-2{\cdot}7\times10^{-2}$
0·23	$6{\cdot}1\times10^{-2}$	$-5{\cdot}8\times10^{2}$	$1{\cdot}7\times10^{2}$	0·83	$-2{\cdot}8\times10^{-2}$
0·41	$1{\cdot}2\times10^{-1}$	$-2{\cdot}5\times10^{2}$	$1{\cdot}1\times10^{2}$	0·79	$-2{\cdot}6\times10^{-2}$
0·54	$1{\cdot}5\times10^{-1}$	$-2{\cdot}0\times10^{2}$	$1{\cdot}1\times10^{2}$	0·73	$-2{\cdot}4\times10^{-2}$
0·72	$2{\cdot}1\times10^{-1}$	$-1{\cdot}5\times10^{2}$	$9{\cdot}5\times10^{1}$	0·73	$-2{\cdot}4\times10^{-2}$
0·97	$2{\cdot}7\times10^{-1}$	$-9{\cdot}5\times10^{1}$	$7{\cdot}2\times10^{1}$	0·62	$-2{\cdot}1\times10^{-2}$

† This value was obtained by vectorially subtracting the cross-spectral values between the velocity and the two pressure signals. The units are (dyn cm^{-2}) (cm s^{-1}) (Hz^{-1}).

‡ $\Delta p = [\overline{\Delta pu}\,\Phi_u^{-\frac{1}{2}}\,(\text{bandwidth})^{\frac{1}{2}}]$ is a magnitude for that part of the pressure difference ($p_{\text{ground}} - p_{\text{air}}$) which is coherent with u and lies within the appropriate bandwidth.

TABLE 2. Vertical pressure gradient at the surface. Data from run 319/1 (see figure 16); $U_5 = 10\,\text{m s}^{-1}$, $u_*^2 = 0{\cdot}4\,\text{m}^2\text{s}^{-2}$.

Data collected using a hot wire for measuring u and the surface pressure measuring technique to obtain p were compared with the results of Gorshkov (1968). When similar spacings were used, the correlation coefficient

$$R_{pu} = \Phi_{pu}/(\Phi_u \Pi)^{\frac{1}{2}}$$

is similar in magnitude to the values he obtained, but of the opposite sign. No explanation is offered for the difference; further study is necessary.

3.5. *Energy transfer by pressure forces*

Two contributions to energy transfer by pressure forces were evaluated. The first represents the net effect of pressure forces in the total energy budget of the atmospheric boundary-layer turbulence. The second is the energy transfer by pressure forces to or from the u velocity component.

The total energy budget at any level for the boundary layer can be approximated by the terms

$$\frac{1}{2}\frac{\partial q^2}{\partial t} = 0 = -\overline{uw}\frac{\partial U}{\partial z} - \frac{1}{2}\frac{\partial}{\partial z}(\overline{q^2 w}) - \frac{1}{\rho}\frac{\partial}{\partial z}\overline{pw} + \text{viscous effects} \qquad (4)$$

(see Lumley & Panofsky 1964, p. 71 ff.), where the first term on the right-hand side is the 'energy feeding' term representing extraction of energy from the mean flow; the second term represents the transfer of turbulent energy by the turbulent velocities ($q^2 = u^2 + v^2 + w^2$); the third term represents the transfer of energy by the pressure gradient–velocity correlation; the final term is the total viscous effect on energy transfer, which is assumed to be entirely dissipation, ϵ. In previous measurements of some of these terms it had been found that the energy feeding term was approximately balanced locally by the viscous dissipation and that the turbulent transfer term was small. The pressure–vertical-velocity term has not been measured directly for a turbulent boundary layer.

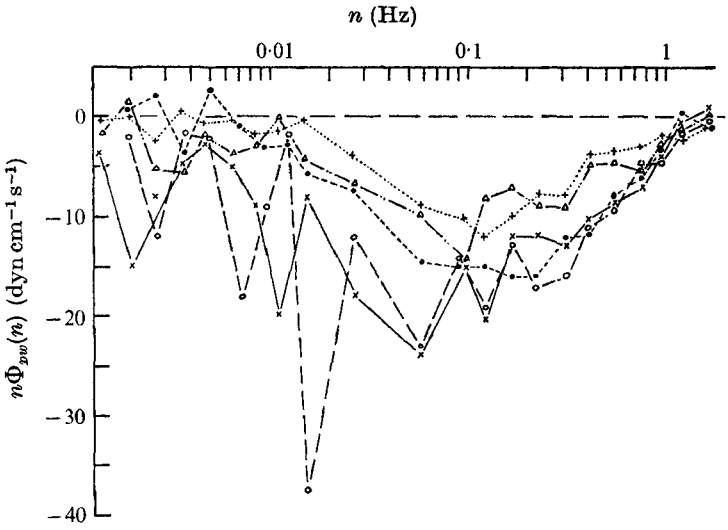

FIGURE 17. Spectra of $\overline{pw}$. ×, run 110/1; ○, run 110/2; ●, run 120/1; △, run 120/2; +, run 121/1.

Because of the approximate balance between local production and dissipation, it had been speculated that the flux divergence by the pressure forces was also small. However, the inaccuracy of such observations makes this method of approximating the flux divergence unsatisfactory and direct measurement is desirable. The measurements required to evaluate the relative importance of the terms in (4) can be simplified by comparing the terms in modified form. Equation 4 is integrated from z_1 to z, where z_1 is a lower level fixed near the 'transition region' (see Hinze 1959, p. 465) where the turbulence is influenced by the viscous effects of the boundary. It is assumed that the 'transition region' is thin and that there is negligible turbulent energy flux through it, the stress being carried by viscous forces. This assumption would only be applicable to observations over a solid surface and not over water when waves are being generated. If these approximations are realistic then the first three terms of the integral are small when evaluated at z_1 compared with those evaluated at z. These assumptions give

$$(-\overline{uw}U)_z, \quad -\tfrac{1}{2}(\overline{q^2w})_z, \quad -(1/\rho)(\overline{pw})_z,$$

each being evaluated at height z, as approximations for the respective three terms representing the budget of turbulent kinetic energy in the space between the boundary and height z. The first term represents the net rate of working per unit area on the surface z by the Reynolds stress $-\overline{uw}$, the second the upward flux of turbulent energy and the third the rate of working per unit area by the pressure force. A comparison of these three terms would indicate the relative importance of each as a net energy source of turbulent kinetic energy per unit area for the air below the level z.

The three terms are compared for five runs each of approximately half an hour in duration. The spectra of $\overline{pw}$ are plotted in figure 17. (Corresponding spectra for p, u, v, w and $\overline{uw}$ are plotted in figures 5(*a*), 9(*a*), 9(*b*), 9(*a*) and 9(*c*)

Run	U_5 (m s^{-1})	z (m)	$-\overline{uw}$ (cm^2 s^{-2})	σ_w/u_*	$-\overline{pw}/\rho$ (cm^3 s^{-3})	$-\frac{1}{2}\overline{q^2w}$ (cm^3 s^{-3})	$-\overline{uwU}$ (cm^3 s^{-3})	$R = \dfrac{\overline{pw}}{\overline{\rho uwU}}$
110/1	7·1	5·5	698	1·32	$6{\cdot}3\times10^4$	$-6{\cdot}5\times10^4$	$50{\cdot}5\times10^4$	0·125
110/2	7·4	4·0	729	1·25	$5{\cdot}5\times10^4$	$-5{\cdot}5\times10^4$	$52{\cdot}5\times10^4$	0·105
120/1	6·5	3·4	580	1·40	$3{\cdot}7\times10^4$	$-2{\cdot}4\times10^4$	$39{\cdot}5\times10^4$	0·095
120/2	6·2	4·8	443	1·47	$2{\cdot}7\times10^4$	$-3{\cdot}9\times10^4$	$29{\cdot}0\times10^4$	0·094
121/1	6·4	1·5	463	1·40	$2{\cdot}3\times10^4$	$-6{\cdot}5\times10^4$	$27{\cdot}0\times10^4$	0·084

TABLE 3. The $\overline{pw}$ term in the boundary-layer energy budget. σ_w = variance of the vertical velocity fluctuations.

respectively.) As seen from figure 17, $\overline{pw}$ is negative or causes energy flux downwards over essentially all scales at which there is a significant Reynolds stress. The values for each of the terms for this group of runs are summarized in table 3. As can be seen, R, the ratio of the rate of working per unit area by the pressure force to that of the Reynolds stress is approximately equal to 0·1 for z between 1·5 and 5·5 m. The run at 1·5 m had some wave generation present, therefore for that run the assumption of no energy flux through the bottom boundary is not completely valid. The net effect of turbulent energy transfer was calculated for the same runs. As can be seen from table 3, the ratio of the turbulent energy flux to $-\overline{uw}U$ is about $-0{\cdot}1$, roughly balancing the $-\overline{pw}$ term, and is again small with respect to the term associated with energy feeding.

The energy budget for the u velocity component in the atmospheric boundary layer can be approximated as

$$\frac{1}{2}\frac{\overline{\partial u^2}}{\partial t} = 0 = -\overline{uw}\frac{\partial U}{\partial z} - \frac{1}{2}\frac{\partial}{\partial z}\overline{u^2w} - \frac{1}{\rho}\overline{u\frac{\partial p}{\partial x}} + \nu\overline{u\nabla^2 u} \tag{5}$$

(see Lumley & Panofsky 1964), where the terms are interpreted in a similar way as those in (4). The other velocity components have similar terms in equations representing their energy budget except for the energy feeding term, which occurs only for the u velocity component. Thus energy extracted from the mean flow is put into the downwind component only. It is the pressure forces which must transfer energy from the downwind component into the two other velocity components.

The energy transferred by the $-u\overline{\partial p/\partial x}$ term was calculated from the simultaneous measurements of u and p. A hot wire positioned about 7 cm to the side of and 4 cm behind the pressure probe was used to measure u. Necessary phase corrections were applied using Taylor's hypothesis. The energy flux was calculated using the quadrature spectrum between u and p. This technique was checked by differentiating the pressure term to obtain $\partial p/\partial x = -(1/U)(\partial p/\partial t)$ and calculating its co-spectrum with u. The two calculations agree within $\pm 10\,\%$. Figures 18(*a*) and (*b*) show the results in non-dimensional form. As can be seen, when integrated with respect to kz between values of 0·05 and 20, the rate of energy loss (per unit volume) from the u fluctuations is about $0{\cdot}3$–$0{\cdot}7\rho u_*^3/(\kappa z)$, where κ is von Kármán's constant.

It would be expected that if data were available for the entire range of

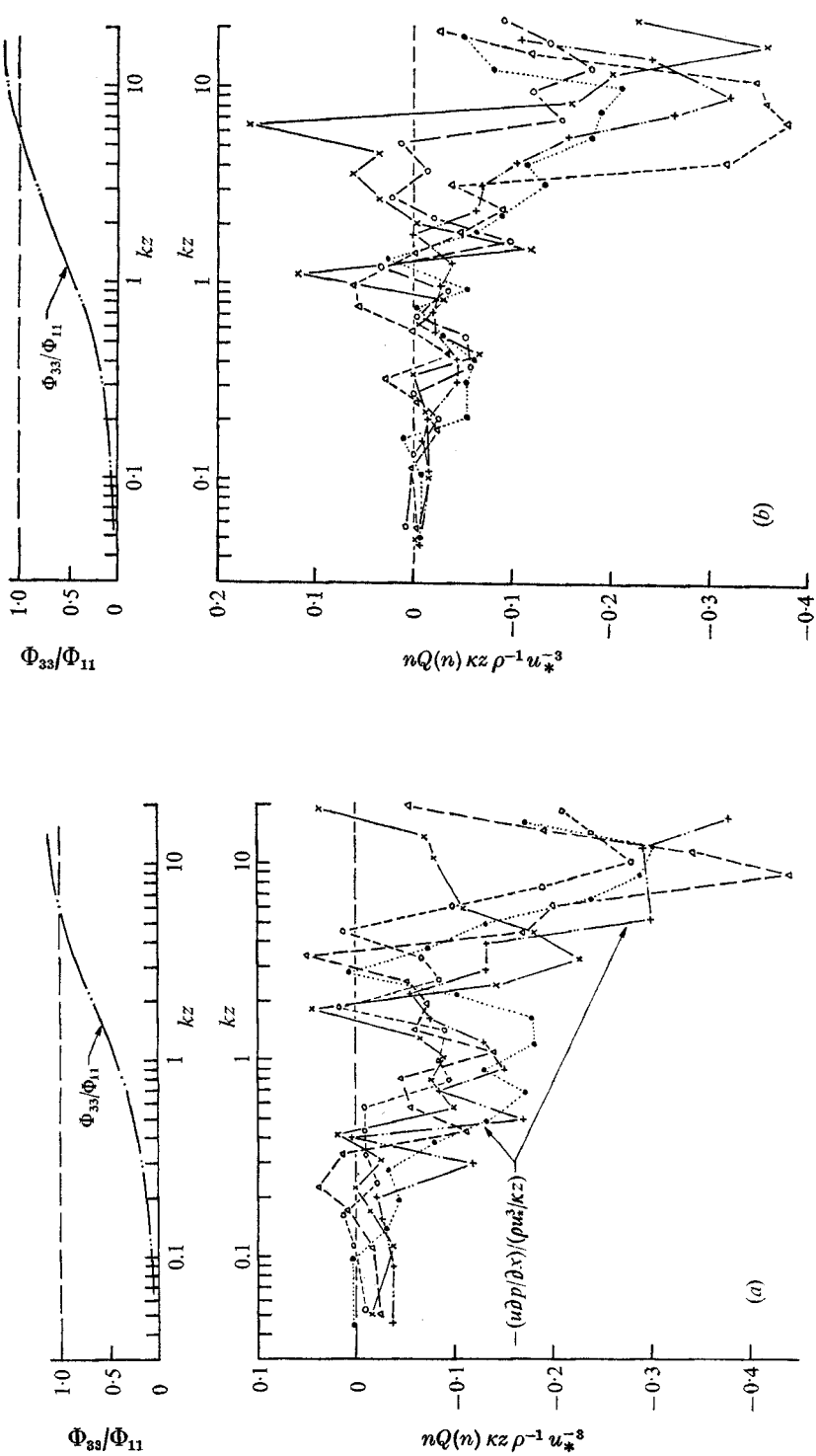

FIGURE 18. Spectral distribution of the energy flux, by pressure forces, from the u velocity component. The integral is for kz from 0·05 to 20. (*a*) ×, run 73/3, integral = −0·38; △, run 72/1, integral = −0·55; ○, run 141/3, integral = −0·41; ●, run 73/1, integral = −0·70; +, run 141/2/2, integral = −0·70. (*b*) ×, run 165/2, integral = −0·28; ○, run 172/2, integral = −0·29; △, run 172/1, integral = −0·51; +, run 173/2, integral = −0·45; ●, run 141/2/1, integral = −0·35.

turbulent scales the integral would have a maximum value of about 0·67, provided that the turbulence eventually becomes isotropic. Both w and v fluctuations are possible sinks for this energy; however, for the scale range observed, the w fluctuations are expected to be the major sink, since w gains energy in this scale range and v has already acquired significant energy at scales larger than those observed. Since the turbulence has not become fully isotropic within the scale range observed, further energy flux is expected for values of kz larger than those observed. For these reasons the integral (the energy loss from the u component) should always be less than 0·67. The relatively large variation in the measured integral, including two variations larger than 0·67, could have resulted from the lack of complete stationarity and the length of the runs being too short for statistical reliability, as is evident from the large variation in shape among the different spectra. The observed energy loss from the u velocity component has a mean value of about $0{\cdot}45\rho u_*^3/\kappa z$; this is more than sufficient to account for that acquired by w fluctuations in this same frequency range.

The energy transfer by $-\overline{u\,\partial p/\partial x}$ can be discussed in terms of two scale ranges. The first, in which energy is lost, is at low values of kz where the w spectra first have appreciable energy. The ratio Φ_{33}/Φ_{11} is shown in figure 18 for comparison. The second range, which contains most of the energy loss measured, occurs just after the peak of the w spectrum, that is, where the turbulence becomes free of the surface (see § 3.4). The energy transfer in most cases drops off towards zero at the high frequencies (i.e. high kz). This is considered to be a real effect rather than being due to probe separation, as can easily be verified using figure 12. It is also evident that for values of $kz < 20$ the turbulence could not be isotropic since there is still significant net energy flux from the u velocity component up to this scale.

From these energy flux measurements it appears that in the total energy budget below 5 m, under neutral conditions, the assumption of a small contribution by the pressure term is reasonable. Not only is the term small but it is also partially balanced by the turbulent flux term. However, for the energy budget of the individual velocity components near the frequency range where the turbulence is carrying the stress, the pressure terms are very important, as expected and as has been shown for the u component.

This work was done as part of the Air–Sea Interaction programme at the Institute of Oceanography, University of British Columbia. While this research was underway the Institute was partially supported by the U.S. Office of Naval Research through Contract NOOO14-16-C-OO47 under Project NR 083-207. The author is grateful for the discussions with and assistance given by Dr R. W. Stewart and Dr R. W. Burling on various aspects of this study. The programming for the data analysis was developed by J. F. Garrett and J. R. Wilson.

Appendix. Data summary

Table 4 lists the 'mean' conditions under which each of the runs mentioned in this report was taken. Some data from unlisted runs were used in the more

Run	Date	Site	Duration (min)	Mean wind at 5 m, U_5 (m s^{-1})	Wind direction (degrees)	Gradient Richardson number, Ri_G	Surface stress, τ (dyn cm^{-2})	Height of observation, z (m)	Mean wind at level of observation, U (m s^{-1})	Mean water depth, h (m)	Mean current, U_w (m s^{-1})
72/1	21 March 1969	SB	18	6·8	270	−0·01	0·650 (2)	2·0	6·5	1·0	0
72/2	21 March 1969	SB	19	6·2	270	−0·02	0·511 (2)	2·0	6·0	1·0	0
73/1	3 April 1969	SB	16	8·2	100	—	0·974 (2)	2·0	7·8	1·0	0
73/2	3 April 1969	SB	10	3·9	260	—	0·287 (2)	3·5	3·9	0	—
73/3	6 April 1969	SB	11	5·5	260	—	0·221 (2)	1·00	4·5	0	—
110/1	8 August 1968	SB	27	7·2	285	—	0·870 (1)	5·5	7·1	0	—
110/2	8 August 1968	SB	26	7·2	285	—	0·910 (1)	4·0	7·4	0	—
120/1	8 August 1968	SB	22	6·8	270	—	0·724 (1)	3·4	6·5	0·75	0·40 W
120/2	8 August 1968	SB	30	6·5	280	—	0·553 (1)	4·8	6·2	1·2	0·40 W
121/1	8 August 1968	SB	27	5·8	275	—	0·479 (1)	1·5	5·4	2·2	0·63 W
141/2/1	3 April 1969	SB	18	7·8	120	−0·01	0·900 (2)	2·0	7·5	1·0	0
141/2/2	3 April 1969	SB	9	7·8	120	−0·01	0·900 (2)	2·0	7·5	1·0	0
141/3	3 April 1969	SB	19	7·6	130	−0·01	0·900 (2)	2·2	7·3	1·0	0
165/2	12 March 1969	SB	13	4·4	280	−0·02	0·277 (2)	2·5	4·3	2·0	0
172/1	20 March 1969	SB	12	5·3	270	−0·04	0·367 (2)	1·5	5·0	1·5	0
172/2	20 March 1969	SB	20	5·9	270	−0·04	0·518 (2)	3·0	5·7	1·0	0
173/1	20 March 1969	SB	19	6·8	280	−0·03	0·611 (2)	2·5	6·5	0·7	0
								4·6	6·8		
173/2	20 March 1969	SB	22	7·4	280	−0·02	0·941 (2)	2·0	7·0	1·0	0·25 W
								2·5	7·1		
186/3	7 April 1969	SB	15	3·6	280	−0·02	0·156 (2)	2·5	3·6	0·5	0
186/4	7 April 1969	SB	9	3·7	270	—	0·196 (2)	3·0	3·6	0	—
								5·1	3·7		

TABLE 4. Mean data for runs

Run	Date	Site	Duration (min)	Mean wind at 5 m, U_5 (m s^{-1})	Wind direction (degrees)	Gradient Richardson number, Ri_G	Surface stress, τ (dyn cm^{-2})	Height of observation, z (m)	Mean wind at level of observation, U (m s^{-1})	Mean water depth, h (m)	Mean current, U_w (m s^{-1})
186/5	7 April 1969	SB	8	2·7	270	—	0·136 (2)	1·25	2·6	0	—
								6·75	2·7		
196/1	15 July 1969	SB	13	3·7	270	−0·12	0·189 (3)	0·46	—	0·20	0
								1·05	—		
196/2	15 July 1969	SB	20	3·4	270	−0·29	0·160 (3)	0·46	—	0·20	0
								1·05	—		
196/3	15 July 1969	SB	8	3·7	270	−0·13	0·189 (3)	0·20	—	0·30	0
								0·76	—		
200/2	17 July 1969	SB	23	4·7	260	−0·01	0·302 (3)	4·0	4·6	2·0	0·64 W
								4·5	4·6		
205/1	19 July 1969	SB	30	3·8	260	−0·04	0·197 (3)	5·0	3·8	1·0	0·30 W
205/2	19 July 1969	SB	23	3·8	260	−0·03	0·197 (3)	5·0	3·8	1·0	0·46 W
318/1	23 August 1969	L	30	4·8	270	—	1·23 (1)	0·40	3·5	—	—
318/2	23 August 1969	L	31	4·8	270	—	1·17 (1)	0·40	3·3	—	—
319/1	27 January 1970	L	24	9·9	270	—	3·84 (2)	0·32	6·7	—	—
319/2	27 January 1970	L	22	9·8	270	—	3·84 (2)	0·32	6·7	—	—
320/1	27 January 1970	L	32	8·8	270	—	1·84 (2)	0·32	6·0	—	—
320/2	27 January 1970	L	29	7·7	270	—	1·16 (2)	0·32	5·3	—	—
425/1	27 January 1970	L	24	6·1	270	—	0·862 (2)	0·32	4·1	—	—
425/2	27 January 1970	L	23	5·2	260	—	0·756 (2)	0·32	3·5	—	—
426/1	27 January 1970	L	32	6·1	270	—	0·862 (2)	0·32	4·1	—	—

TABLE 4 (*cont.*)

general summary plots; conditions were similar to those shown. The runs are in numerical order.

The site abbreviations used are SB for Spanish Banks and L for Ladner. The 'duration' is the total time, in minutes, of digitized data. Most of the runs were originally about half an hour in duration; however, instrument saturation or drift often necessitated using shorter pieces of data for analysis. The value for the stress $\tau = 1{\cdot}25 \times 10^{-3} u_*^2$ is followed by a number (1, 2, or 3) in brackets. This number indicates the method used to evaluate the stress: (1) for direct measurement, (2) for the Φ_{11} method, and (3) for the drag coefficient. If two instruments at different levels were used, the heights above the surface (or mean water level) are given in succeeding lines. The water current at the Spanish Banks site generally flowed in an east–west direction. Listed after the magnitude of the current is the directions given as E for a current flowing *from* the east and W for flow *from* the west. For observations over water, the winds have been referenced to a co-ordinate system moving with the mean current.

REFERENCES

Batchelor, G. K. 1960 *The Theory of Homogeneous Turbulence.* Cambridge University Press.

Blackman, R. B. & Tukey, J. W. 1959 *The Measurement of Power Spectra.* Dover.

Blake, W. K. 1970 *J. Fluid Mech.* **44**, 637.

Bradshaw, P. 1967 *J. Fluid Mech.* **30**, 241.

Bull, M. K. 1967 *J. Fluid Mech.* **28**, 719.

Elliott, J. A. 1970 Ph.D. dissertation, Institute of Oceanography, University of British Columbia.

Fiedler, F. & Panofsky, H. A. 1970 *Bull. Am. Meteor. Soc.* **51**, 1114.

Golitsyn, G. S. 1964 *Izv. Geophys. Ser.* **8**, 1253. (See also *Trans. Am. Geophys. Un.* **8**, 761.)

Gorshkov, N. F. 1967 *Izv. Atmos. Oceanic Phys.* **3**, 447. (See also *Trans. Am. Geophys. Un.* **3**, 255.)

Gorshkov, N. F. 1968 *Izv. Atmos. Oceanic Phys.* **4**, 460. (See also *Trans. Am. Geophys. Un.* **4**, 259.)

Gossard, E. E. 1960 *J. Geophys. Res.* **65**, 3339.

Herron, T. J., Tolstoy, I. & Kraft, D. W. 1969 *J. Geophys. Res.* **74**, 1321.

Hinze, J. O. 1959 *Turbulence.* McGraw-Hill.

Kraichnan, R. H. 1956 *J. Acoust. Soc. Am.* **28**, 378.

Lumley, J. L. & Panofsky, H. A. 1964 *The Structure of Atmospheric Turbulence.* Interscience.

McBean, G. A. 1971 *Boundary-Layer Meteor.* 1, 438.

Pond, S., Smith, S. D., Hamblin, P. F. & Burling, R. W. 1966 *J. Atmos. Sci.* **23**, 376.

Priestley, J. T. 1965 *N.B.S. Rep.* no. 8942.

Stewart, R. W. 1969 *Radio Sci.* **4**, 1269.

Townsend, A. A. 1955 *The Structure of Turbulent Shear Flow.* Cambridge University Press.

Weiler, H. S. & Burling, R. W. 1967 *J. Atmos. Sci.* **24**, 653.

Willmarth, W. W. 1958 *J. Aeron. Sci.* **25**, 335.

Willmarth, W. W. & Wooldridge, C. E. 1962 *J. Fluid Mech.* **14**, 187.

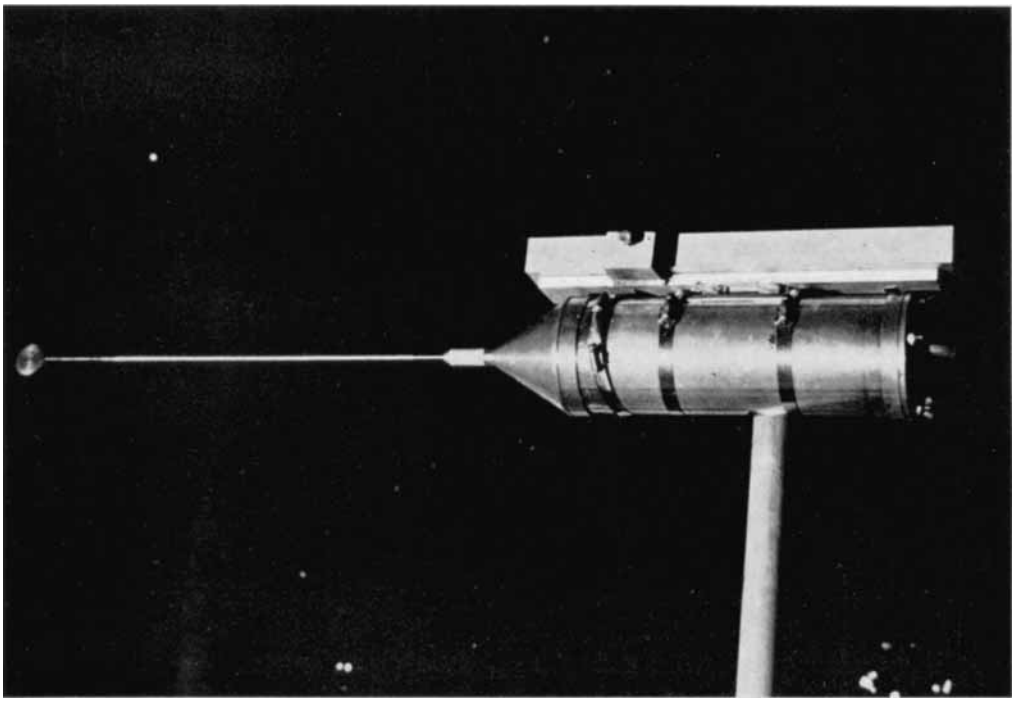

FIGURE 1. View, from above, of the pressure instrument used to measure the static pressure fluctuations. The diameter of the disk, seen at the far left, is about 4 cm.